January 1999

Re: EOARD Special Contract Program SPC 97-4067

Effect of Sideslip on the Flow over a 65-deg Delta Wing; Final Report

by

N.G. Verhaagen
Delft University of Technology
Department of Aerospace Engineering
P.O. Box 5058, 2600 GB Delft
The Netherlands
n.g.verhaagen@lr.tudelft.nl

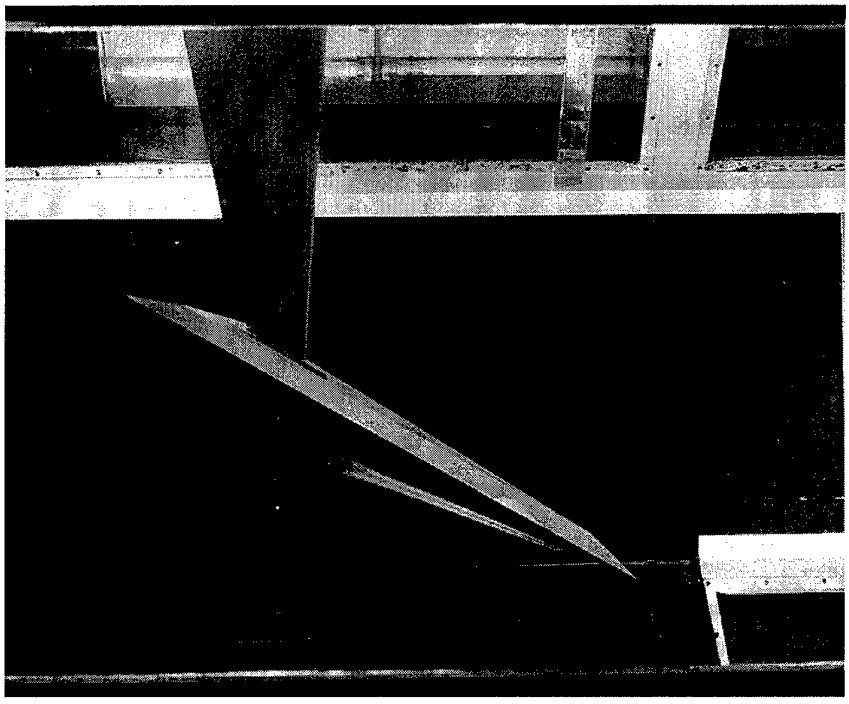

REPORT DOCUMENTATION PAGE

Form Approved OMB No. 0704-0188

1. AGENCY USE ONLY (Leave blank)	2. REPORT DATE	3. REPORT TYPE AND DATES COVERED
	January 1999	Final Report

4. TITLE AND SUBTITLE

Effect of Sideslip in the Flow over a 65-Deg Delta Wing

5. FUNDING NUMBERS

F6170897W0239

6. AUTHOR(S)

Prof. Nicolaas Goris Verhaagen

7. PERFORMING ORGANIZATION NAME(S) AND ADDRESS(ES)

Delft University of Technology
Dept. of Aerospace Engineering
PO Box 5058
Delft 2600 GB
Netherlands

8. PERFORMING ORGANIZATION REPORT NUMBER

N/A

9. SPONSORING/MONITORING AGENCY NAME(S) AND ADDRESS(ES)

EOARD
PSC 802 BOX 14
FPO 09499-0200

10. SPONSORING/MONITORING AGENCY REPORT NUMBER

SPC 97-4067

11. SUPPLEMENTARY NOTES

12a. DISTRIBUTION/AVAILABILITY STATEMENT

Approved for public release; distribution is unlimited.

12b. DISTRIBUTION CODE

A

13. ABSTRACT (Maximum 200 words)

This report results from a contract tasking Delft University of Technology as follows: The contractor will investigate in detail the Effect of Sideslip in the Flow over a 65-deg Delta Wing. He will perform balance measurements as well as on and off the surface flow visualization.

14. SUBJECT TERMS

EOARD, Aircraft Subsystem, Control System

15. NUMBER OF PAGES

60

16. PRICE CODE

N/A

17. SECURITY CLASSIFICATION OF REPORT	18. SECURITY CLASSIFICATION OF THIS PAGE	19, SECURITY CLASSIFICATION OF ABSTRACT	20. LIMITATION OF ABSTRACT
UNCLASSIFIED	UNCLASSIFIED	UNCLASSIFIED	UL

Abstract

Flow-visualization tests, surface-pressure measurements and balance tests were conducted on a model of a flat-plate 65-deg swept delta wing in a low-speed wind tunnel. The model was tested at a fixed angle of attack of 30 deg and at angles of sideslip up to 20 deg. The tests generated data that were used to study the effect of sideslip on the flow over the delta wing.

Contents

1 Nomenclature

b	wing span
B	tunnel span
c	root chord length
C	tunnel cross-sectional area
C_D	drag coefficient
C_l	rolling-moment coefficient
C_{l_β}	lateral stability derivative
C_L	lift coefficient
C_m	pitching-moment coefficient, about $x = 0.775\ c$
C_n	yawing-moment coefficient, about $x = 0.775\ c$
C_N	normal-force coefficient
C_p	static-pressure coefficient
C_Y	lateral-force coefficient
H	tunnel height
q	freestream dynamic pressure
Re	Reynolds number, based on root chord length
s	local wing semispan
S	wing area
t	wing thickness
V	wing volume
x, y, z	coordinates of wing axes system, origin at apex
x_p, y_p	coordinates of center of pressure
α, AoA	angle of attack
β, AoS	angle of sideslip
ϕ	angle of roll

2 Introduction

Modern fighter aircraft are designed to rely on the lift generated by vortex flow to enhance maneuverability. Strong vortices generated at the leading edge of highly-swept lifting surfaces are part of the overall flowfield of such aircraft. At angle of attack and sideslip these leading-edge vortices have a dominant effect on the flow and the airloads. At high angles of attack a sudden change in the vortex flowfield occurs when the core of a the vortex bursts over the wing surface. This change in flow structure causes strong nonlinearities in the aircraft's aerodynamic behavior. The aerodynamics at these conditions depend on time and motion history [1], [2].

Studies of the flow phenomena occurring at near- and post-stall conditions are essential to meet the requirement of increasing maneuverability of current and future fighter. At the Air Vehicles Directorate of the Air Force Research Laboratory (AFRL) and the Institute for Aerospace Research (IAR) of the National Research Council of Canada studies are conducted to help develop mathematical models which simulate aerodynamic nonlinearities encountered during dynamic flight conditions. Several wind tunnel studies were conducted on a rolling 65-deg swept delta wing (Fig. 1). The model has sharp leading and trailing edges which are symmetrically beveled at an angle of 20 deg. Most data were taken at a Mach number of 0.3 and a chord Reynolds number of 3.6 million. The model was tested on a sting at an angle of 30 deg. The tests indicate the existence of critical states at roll angles ϕ of about 5, 8, 11.3 and 18 deg (Fig. 2). A critical state is characterized by a discontinuity in the static force-and-moment curves. If a critical state is encountered, time is required for the transition from one flow state to the other. The test data confirm the existence of strong nonlinearities in the forces and moments and a dependency on the motion history. The critical states are important to flight mechanics. A nonlinear indicial response theory is developed to simulate the aerodynamic nonlinearities near the critical states.

Huang, et al, [1] conducted extensive flow visualization tests to study the changes in the flow topology under static conditions associated with the critical states. Several characteristic surface patterns were identified and based on these patterns possible corresponding three-dimensional flowfield topologies. Discussions with research engineers from AFRL have learned that the interpretation of the surface patterns was complicated by the beveling of the model and the presence of a tangent-ogive centerbody [3]. Ericsson [4] has shown that a center body induces an effective camber which affects the onset of vortex burst. This raises the question to what extent geometrical parameters like beveling and centerbody size do contribute to aerodynamic nonlinearities. This could be investigated by studying the aerodynamic characteristics of a series of models of different cross-sectional shape. Before starting such an extended program, in the frame of the present EOARD Special Contract, a study has been conducted using two models of a simple flat-plate 65-deg delta wing. The models were constructed at the Delft University of Technology (TUD) and tested there in the Low-Turbulence-Tunnel (LTT).

The objective of the present tests was to study the changes in the flow over the wing due to sideslip. In addition, to identify nonlinearities, if any, in the aerodynamic data. Huang, et al, [1] carried out their tests with a rolling model. A rotation about the roll axis of the model is not possible with the current model support system in the LTT. The

models were tested therefore at various angles of sideslip. According to Fig. 2, the flow phenomena occurring over the delta wing at roll also take place over the wing at sideslip.

The present report gives an overview of data available from earlier publications, describes the setup, corrections and results of the present testings, and discusses the effect of sideslip on the aerodynamic data of a flat-plate 65-deg delta wing.

3 Earlier Research Data

One of the earlier studies of the effect of the angle of sideslip on the lateral stability of a flat-plate 70-deg delta wing was conducted by Johnson, et al, [5] in wind tunnels at NASA Langley back in 1980. Their model had a span of 894.1 mm. No further details of the model are given in their paper. The authors noted a fundamental difference in the variation of the lift coefficient C_L and rolling-moment coefficient C_l with the angle of sideslip between low and high angle-of-attack conditions (Fig. 3). At $\alpha = 16$ deg, the C_L shows a small decrease with β, while at $\alpha = 36$ deg, this coefficient initially decreases strongly and then more gradually with β. The C_l shows a linear variation with β at low α, but a strong non-linear variation with β at high α. The occurrence of vortex breakdown over the wing has an important influence on the behavior of the force-and-moment curves. Fig. 4 shows the boundaries for the burst at the leading- and trailing-edge on the windward side of the wing. It is not clear from the latter figure what the exact chordwise location of the burst is at the leading edge. In any case, it is not at the apex of the wing. At $\alpha = 16$ deg burst occurs over the windward side beyond $\beta = 10$ deg, but at $\alpha = 36$ deg the vortices are burst over the major part of the wing already at $\beta = 0$ deg. As indicated in Fig. 5, the abrupt loss in lift and reversal of the slope in the C_l-curve at small β is thought to be due to the upstream movement of the windward bursting point and downstream displacement of the burst over the leeward wing side. The large lift loss at small β is mainly due to the breakdown of the windward vortex, while the variation in vortex breakdown over the left and right wing sides produces a positive lateral stability derivative C_{l_β}. When β increases beyond 4 deg, C_{l_β} becomes negative. According to Johnson, et al, [5] this is due to the leeward vortex moving off the wing. Fig. 6 compares the C_{l_β} for β in the range between -4 and +4 deg with values estimated with the linear theory of Hoak [6]. The measured values can be seen to deviate strongly from the estimated values beyond $\alpha = 20$ deg. Positive values for C_{l_β} were measured only in a small range near $\alpha = 36$ deg.

McKernan and Nelson [9] of the University of Notre Dame also studied the effect of sideslip on the data of 70-deg delta wings. They tested two similar wings, one with pressure taps, and the other without, in an open-circuit tunnel with a square test section, 0.61-m wide and 0.61-m high. The models had a chord length of 406.4 mm, a span of 296 mm and a thickness of 19 mm, yielding a thickness-to-chord ratio of 0.047. The chord Reynolds number was 0.225 million. Fig. 7 shows the effect of β on the burst point of the windward vortex at various α. The data confirm the trend of Fig. 4 that the windward vortex burst moves upstream with increasing angle of attack and sideslip. Fig. 8 shows plots of the rolling moment as a function of β at various α. The derivative C_{l_β} for β between -4 and +4 deg calculated from these plots is given in Fig. 9. Similar to the data of Johnson, et al, the derivative decreases up to $\alpha = 20$ deg, the angle where the windward vortex starts to burst over the wing. At larger angle of attack, C_{l_β} increases as the burst on the windward side moves towards the apex. Beyond $\alpha = 35$ deg, the curve reverses again because the leeward vortex burst has reached the wing and will move towards the apex at larger α. This reversal of the rolling moment curve causes a phenomenon known as wing rock.

Verhaagen and Naarding [7] studied the effect of sideslip on the characteristics of a

76-deg biconvex delta wing. The data were obtained in a wind tunnel at a constant $\alpha =$ 21 deg and a chord Reynolds number of 2.5 million. As shown in Fig. 10, vortex burst was observed to occur on the windward side of the wing beyond $\beta = 12$ deg. Fig. 11 shows the effect of β on the spanwise pressure distribution at x/c = 0.60. Fig. 13 illustrates the effect on the force-and-moment curves. Up to $\beta = 12$ deg, the suction on the windward side increases with sideslip due to the fact that the vortices increase in strength and draw closer to the upper surface. The trends on the leeward side are opposite, the vortices move away from the upper surface, reducing the suction with increasing sideslip. Up to β = 12 deg, the normal-force coefficient C_N reduces slightly with increasing sideslip angle. This is due to a slight reduction of the loading on the rear part of the wing. Associated with this is a gradual increase of the pitching-moment coefficient C_m. The increasing asymmetry of the spanwise pressure distribution results in a more negative value for C_l. Beyond $\beta = 12$ deg, vortex burst occurs over the windward side. The upstream influence of this phenomenon results in a decrease of the suction when the angle of sideslip increases to 20 deg. The effect of burst is very clear at stations near the trailing edge (Fig. 12). Downstream of the burst the suction peak decreases in level and extends in the lateral direction due to the fact that the flow behind the burst core becomes turbulent and extends in the radial direction. The effect of the burst on the balance data is a discontinuity in the force-and-moment curves at $\beta = 12$ deg. The suction on the leeward side reduces to low values at large angles of sideslip. The vortex moves off the wing at approximately β = 14 deg (= semiapex angle).

4 Experimental Setup and Conditions

4.1 Wind Tunnel

The tests were conducted in the LTT of the low-speed windtunnel laboratory of TUD. This is a closed-circuit tunnel with a octagonal test section 1.80-m wide, 1.25-m high and 2.60-m long. Turntables of 1.15-m diameter are fitted in the upper and lower walls. A high contraction ratio (17.9) and a large number of screens result in a good flow quality and a low turbulence level. The longitudinal component of the turbulence increases from 0.025% at 40 m/sec to 0.085% at 100 m/sec. The capabilities of the LTT and its equipment for generating aerodynamic data on the flow over delta wings, with and without sideslip, have been shown in references [7] and [8].

4.2 Models

Two flat-plate Duraluminium 65-deg swept delta wings constructed at TUD were used for the tests. As shown in Fig. 14, the wings have a chord length of 0.665 m and a semispan of 0.620 m. Their thickness equals 20 mm, yielding a thickness-to-chord ratio t/c of 0.03. The leading and trailing edges are sharp and beveled at the under surface at 30 and 22 deg, respectively. Each model was suspended at the x = .515 m (77.5% chord) position through a streamlined strut connected to the balance system overhead the test section (Fig. 15). Struts are available which enable the wings to be rotated either about their pitch or yaw axis. For measurements at zero yaw, the angle-of-attack range is from -25 to +25 deg. For yaw measurement, struts are available that keep the wing at a fixed α. To approach the test conditions of Huang, et al [1], the α = 30 deg strut was used for the present tests (the test results will show that a lower-α strut would have been better). To avoid interference of the strut with the vortex flow, the wings were tested inverted, i.e. with their flat surface facing down. It is common to present data of delta wings with their leeward surface facing up. This surface is then called the "upper" surface. This terminology will also be used in this report.

One wing was used for the balance measurements and flow-visualization tests, while the other one - provided with pressure taps - was used for the surface-pressure recordings. Fig. 16 shows a picture of the latter wing when it was in the construction workshop. The picture was taken prior to the installation of the pressure tubes into the 33 grooves that were milled into the bottom surface of the model along rays through the apex. In the pressure tubes taps were drilled from the upper surface of the wing on 15 spanwise rows, from x/c = 0.05 to 0.99. The distribution of the taps on the left and right side of the wing is identical. Table 1 gives the distribution of the taps on the flat upper surface (a tap is marked by a $\odot$ symbol). At x/c = 0.75 and 0.80 no taps were drilled at y/s = 0 and 0.10, because the presence of a strut/wing pivot block at this location made this impossible. After the installation of the pressure tubes, the grooves were filled with a "jelly" consisting of resin and Aluminium particles mixed with hardener. When solid this was sanded to a flat and smooth bottom surface. On this surface, taps were drilled on 3 spanwise rows, located at x/c = 0.30, 0.50 and 0.70 (Table 2). Fig. 17 shows a picture of the wing in the LTT.

The measurements were conducted at β ranging from -20 to +20 deg and an airspeed of 50 m/sec. This corresponds to a Reynolds number of 2.3 million, based on chord length. Preliminary tests indicated that the model and its support started to suffer from low amplitude, but high frequent oscillations at airspeeds over 50 m/sec. These are induced by the highly unstable flow occurring over the model at high angles of attack and sideslip. To avoid any damage to the model, the tests were not performed at a higher speed.

4.3 Flow Visualization

Prior to the flow visualization tests, the upper surface of the wing was covered with black vinyl contact paper to enhance the contrast. The high airspeed and large angle of attack generated very low pressures and temperatures in the unburst cores of the leading-edge vortices. As a result, natural condensation occurred in these cores making it possible to observe their trajectory and bursting location with the naked eye (see picture on front page 1). Photo lamps located on the bottom and sides of the test section were used to extra illuminate the vortex cores. Still photographs were taken through a window in the floor of the test section at both positive and negative β using a Hasselblad 500 EL camera with 125 ISO black-and-white film, and an Olympus OM-2 camera with 100 ISO color-slide film. Exposure time varied between 1/4 to 2 sec depending on the aperture setting. Video recordings of the vortex core burst were taken to study the dynamics of the vortex flow.

The flow pattern on the upper surface of the wing was visualized using two mixtures, viz. an oil-flow mixture consisting of titanium dioxide and kerosene, and a mixture of fluorescent-dye and oil. The mixtures were applied to the wing and the airspeed in the test section was brought up to the test conditions as fast as possible.
In the case of the oil-flow mixture, after this mixture had dried completely, the contact paper was removed from the wing, put on card board and photographed on black-and-white film. The patterns were visualized at β ranging from 0 to 10 deg. No larger β was visualized to avoid too much contamination by the oil of the diffuser and corner vanes of the wind tunnel.
The surface pattern visualized with the fluorescent-dye/oil mixture was illuminated using ultraviolet light. This mixture has the advantage that it does not dry while the tunnel is running, making it possible to study the changes to the surface pattern with running time. In addition, it is possible to observe the variations to the surface pattern due to yaw. After some running time most of the fluid accumulated near the separation lines and singularities, leaving little fluid to visualize the streamline pattern on the wing. To avoid this, a lower airspeed of 39 m/s was used for these tests. The corresponding chord Reynolds number was 1.7 million. The airspeed had nevertheless to be brought back to zero from time to time to manually redistribute the mixture over the wing surface. Color-slides of the patterns were taken at β from zero up to 20 deg.

4.4 Surface-Pressure Recordings

Surface-pressure data were obtained by consecutively recording the pressures at each of the 18 spanwise rows of taps. The taps in each of the 33 pressure tubes are mutually

connected through the tube. The spanwise pressure distribution at a specific row was therefore recorded by sealing off the taps of the other 17 rows with strips of thin adhesive tape. The pressure tubes were led out of the model through a streamlined tube at it's back end and were connected to a multiple manometer of 200 tubes. The level of the fluid in the tubes was recorded automatically and stored on disk. The manometer records static time-averaged values for the pressure with an accuracy of $\pm$ 1 Pa.
The surface-pressure data were taken at β from +20 to -20 deg, in steps of 1 deg. Additional runs were carried out to check the repeatability of the data. For this report only the data taken at positive β were processed.

4.5 Balance Measurements

Balance measurements were performed using a six-component balance system (platform type) with automatic weigh-beams of high accuracy. The measurements provided static time-averaged force-and-moment data. With the wing inverted, the following three data sets were measured:

set	**β range (deg)**
1	-20 (1.0) +20, +20 (1.0) -20
2	-20 (0.5) +20, +20 (0.5) -20
3	-10 (0.1) +10, +10 (0.1) -10

In the first and second set, the wing was yawed from -20 to +20 deg and back again, in steps of 1 and 0.5 deg, respectively. The measurements were conducted with increasing and decreasing β to obtain information on the hysteresis of the data. The flow visualization studies, conducted prior to the balance measurements, showed that between β = -10 and +10 deg important changes occurred in the flow over the delta wing. To be able to study in detail the effect of these changes on the data in this β-range, in the third set steps of 0.1 deg were used.

5 Corrections

5.1 Tunnel Wall Interference

The presence of tunnel walls causes the flow around the wing to be different from that in free air. The wing, its support and wake reduce the effective cross section of the tunnel. Associated with this so-called blockage effect is an increase in the dynamic pressure of the flow around the wing. The walls also impose a constraint on the downward (and in case of sideslip lateral) deflection of the wake. This affects the angularity of the flow around the wing. Additional effects are due to lift interference, which is associated with the circulation around the wing and changes the effective flow angles and the surface-pressure distribution of the wing.

An overview of existing wall-correction theories for wings with leading-edge separation has been given by the author of this report in Ref. [10]. No theory was found that predicts the wall interference effects on the aerodynamic characteristics of delta wings at angles of attack over 25 deg, or when vortex burst occurs over the wing. Nor was a theory found that predicts the wall effects on the flow over a delta wing at sideslip. The best way to obtain an idea of the order of magnitude of the wall interference, is to consider the theory developed by Hsing and Lan [11]. Their theory takes into account the interference effect of a large viscous wake such as present behind the delta wing tested here. They use a thin-layer Navier-Stokes solver to simulate the flow about a delta wing at angle of attack in a wind tunnel. The computed wall-pressure distribution is used as the boundary condition for an Euler solution of the wind tunnel flow without the delta wing. The computed interference flowfield is used to estimate blockage and upflow effects. Based on the solutions for a wing-body/strake configuration in tunnels of different cross-sectional dimensions, Hsing and Lan derived the blockage and upflow correction charts shown in Fig. 18. The interference parameter ICP used in these charts is defined as:

$$ICP = (S/C)/(H/B)$$

where S is the wing area, C is the tunnel cross-sectional area, and H/B the tunnel height-to-span ratio. The charts are valid for angles of attack up to 25 deg, or up to angles where vortex burst takes place over the wing. Support interference effects were not included in the solutions. For the present tunnel and delta wing:

$$S = 0.206 \text{ m}^2,\ C = 2.250 \text{ m}^2 \text{ and } H/B = 0.694, \text{ so that } ICP = 0.132.$$

Extrapolation of the data of Fig. 18 to this value for ICP and to $\alpha = 30$ deg is problematic, because it is unknown how the flow in the tunnel and hence the blockage and upflow will behave beyond the upper limit $\alpha = 25$ deg and $ICP = 0.091$ of Fig. 18. At the latter values the blockage is in the order of 7%, while the upflow angle is about 3 deg. At the test α and ICP, the upflow angle might be as large as 5 deg. As far as the wall interference effects on the angle of sideslip are concerned, as said before, no theory was found to help estimate these effects. It can be expected, however, that the constraint of the walls on the lateral deflection of the viscous wake will have an influence on the effective angle of sideslip.

5.2 Balance Data

The balance data were corrected for the elastic deformation of the strut and balance system under aerodynamic load. The deflections increase the angle of attack to a value of 31.4 deg at zero sideslip, and to 30.8 deg at β = +/-20 deg. The effect of the deflections on β is much smaller and of the order of 0.01 deg at the largest β.
The balance data were also corrected for strut/model interference effects. These were determined from testings obtained on the model with its flat surface facing up, with and without a dummy strut.
The force coefficients are based on dynamic pressure and wing area, the moment coefficients are in addition based on chord (C_m) or span (C_l and C_n) as reference length. The moments are given in the wing-axes system, relative to the strut/model pivot location at $x/c = 0.775$. Usually, these moments are given relative to a different location, such as the mid chord or quarter mean-aerodynamic-chord. To calculate the moments relative to such a location, a summation or substraction of moments is necessary. Since such a manipulation increases the error, this has been omitted here.
As far as tunnel wall interference is concerned, the force-and-moment coefficients were corrected for a blockage of 7%.

5.3 Surface-Pressure Data

The static-pressure coefficient C_p was calculated from the difference between the pressure recorded at a tap and the freestream static pressure, non-dimensionalized by the freestream dynamic pressure. To the latter pressure a blockage correction of 7% was applied.

5.4 Angle of Attack

Although the angle of attack of the wing was exactly 30 deg at zero airspeed, the elastic deformation of the strut and balance system under aerodynamic load increased α to a value of 31.4 deg at zero sideslip, and to 30.8 deg at β = -/+20 deg. As discussed in Section 5.1, the tunnel-wall-interference effects are estimated to be responsible for an upflow angle in the order of 5 deg. This all means that during the tests the effective angle of attack could have been as large as 36 to 37 deg. In hindsight, to approach the test conditions of Huang, et al [1], it would have been better to set the angle of attack at a value of 25 instead of 30 deg at zero airspeed.

6 Test Results

6.1 Off-Surface Flow Visualization

Still photographs of the condensed cores were taken at β from -8 to + 8 deg, in steps of 1 deg. Exposure times were used that varied between 1/4 and 2 sec. As an example, Fig. 19 shows pictures of the core trajectory and bursting location at $\beta = 0$, 2 and 4 deg, while the locations at $\beta = +6$ and -6 deg are shown in Fig. 20. From the photographs the mean bursting location was determined. The bursting point was defined to coincide with the location where the core was observed to expand. Downstream of this location the core diffuses rapidly. The change of the burst with positive β (or AoS) is given in Fig. 21. It should be remarked here that tunnel-wall-interference not only affects the angle of attack and sideslip, but also the burst location. The effect of the tunnel walls on the burst location over delta wings was studied by Weinberg [12], Lowson and Riley [13], and Pelletier and Nelson [14]. Surprisingly, the conclusions of their studies are far from unique. The bursting point was observed either to move downstream [12], to remain unaffected [13], or to move upstream [14] with increasing wing size!

The burst on the leeward wing side (off-the-wind) moves into the downstream direction with increasing β, the burst on the windward side moves towards the apex. The cores on the latter side remained visible up to $\beta = 3$ deg, the cores on the other side up to $\beta = 8$ deg. The effective leading-edge sweep increases with β on the leeward side, and decreases with β on the windward side. Keeping this in mind, it can be said that the tendency shown in Fig. 21 corresponds to that of Wentz and Kohlman [15], and of Huang, et al, [16]. These investigators observed that an increase of the leading-edge sweep of a flat-plate delta wing tends to increase the distance from the bursting point to the apex. On the present wing not much difference was observed between the chordwise location of the burst at positive and negative angle of sideslip (Fig. 20).

The video recordings were used to estimate the amplitude and frequency of the oscillation of the burst along the core axis. The estimated range of the burst locations at each β is marked by error bars in Fig. 21. The amplitude of the oscillations tends to increase with sideslip. The bursts were observed to oscillate at a frequency of 4 - 5 Hz. Beyond $\beta = 5$ deg, the condensation along the entire core started to become interrupted with about the same frequency. The intermittent condensation of the core may be due to an instability in the formation of the vortex near the apex. Associated with this streamwise instability was a loud flapping noise that started to become audible in the tunnel at $\beta = 6$ deg and disappeared again at $\beta = 12$ deg. The cause of this instability is not clear and needs further investigation.

Menke and Gursul [17] found that the oscillation of the bursts over a 75-deg delta wing at a constant $\alpha = 29$ deg was caused by the interaction of the windward and leeward burst. Amplitudes were recorded of 10% chord at a Reynolds number of 41,000. They tested their wing in a water tunnel. Mitchell, et al, [18] confirm that the oscillation of the burst is due to the interaction with the burst on the opposite wing side. They tested a 70-deg delta wing in a wind tunnel at various α and airspeed, and found the amplitude of the

burst oscillation to depend on these two parameters.
From other experiments it is known that at least two primary types of vortex breakdown can be distinguished; the spiral- or the bubble-type of breakdown. Unfortunately, the temporal resolution of the video recordings was not detailed enough to identify the type of breakdown occurring at the present test conditions.

6.2 Surface-Flow Visualization

Fig. 22 shows pictures of the upper-surface streamline pattern for $\beta = 0$ and 10 deg, as visualized with the oil-flow mixture consisting of titanium dioxide and kerosene. Figs. 23 and 24 show pictures of the patterns at β from 1 to 20 deg, as visualized with a second mixture consisting of fluorescent-dye and oil. The latter black-and-white pictures were obtained by scanning coloured prints of the slides taken during the tests. The resolution of the black-and-white pictures shown, unfortunately, is far less than that of the coloured prints.

For practical reasons, instead of 50 m/sec an airspeed of 39 m/sec was used during the application of the second visualization technique. This difference in speed is believed to only affect the location of the boundary-layer transition region. This region is characterized by a kink in the secondary-separation line that is caused by an outboard shift of this line. This shift is a consequence of the transition of the boundary layer from laminar to turbulent. At $\beta = 0$ deg, the kink is located at approximately $x/c = 0.17$ when the airspeed is 50 m/sec, and at $x/c = 0.30$ when the speed is 39 m/sec. This tendency is known from other experiments; a reduction of airspeed (or Reynolds number) increases the distance from the boundary-layer transition region to the apex [19].

Based on the pictures given in Figs. 22 to 24, the conjectured surface-flow topology at various β is sketched in Figs. 26 and 27. A long-dash-dot line marks the centerline of the wing, while solid lines indicate surface streamline or skin-friction lines, and attachment and secondary-separation lines. The pattern that is formed by the skin-friction lines can be considered as a continuous vector field in which singular (or critical) points occur where the skin friction is zero. In a recent paper Jobe, et al, [20] discuss the topology of flows and give a survey of literature on this subject. As shown in Fig. 25, singular points can be classified as saddle points or nodes. Through a saddle point (S) pass only two skin-friction lines (the critical lines). The direction of the shear on either side of the saddle point are inward on one critical line and outward on the other critical line. All the other skin-friction lines miss the singular point and take directions consistent with those of the adjacent critical lines. Through a node an infinite number of skin-friction lines pass, either all into or all out of the singular point. Nodes can be subdivided into nodal points and foci. At a nodal point two straight critical lines pass through the singular point. All skin-friction lines are either directed outward away from the node (a nodal point of attachment N_a) or inward toward the node (a nodal point of separation N_s). The other type of node, the focus, has no common tangent line. All skin-friction lines spiral around a singular point, either out of it (a focus of attachment N_{f_a}) or into it (a focus of separation N_{f_s}).
A basic topological rule for the skin-friction line pattern is that the number of nodal points should exceed the number of saddle points by two. This rule can not been applied to the

skin-friction patterns given in Figs. 26 and 27, because the singularities at the nose and trailing edge are not specified. The topology of the flow in these regions is complex and will need further study. In Fig. 3 of Ref. [20] possible skin-friction line patterns for the nose region of a delta wing are given. The flow near the nose was assumed to be similar to that at the nose of a round-nosed wing.

The skin-friction patterns show that the boundary-layer transition region on the windward side moves towards the apex with increasing β. On the leeward side, this region moves into the opposite direction. The kink in the secondary-separation line can be detected up to $\beta = 7$ deg. Upstream of the transition region, a tertiary-separation line is visible between the leading edge and the secondary-separation line (the tertiary-separation line has not been drawn in Fig. 26). Downstream of the transition region, the secondary-separation line moves slightly inboard. From $\beta = 4$ deg, a small whorl adjoining the secondary-separation line becomes visible near the leeward tip. The skin-friction lines in this region spiral inward around a center, indicating that topologically this is a focus of separation. Between the focus and the trailing edge, a saddle point can be expected. Due to the abundance of the oil at the tip, this is not evident from the pictures. Topologically, Earnshaw and Lawford [21] found similar whorls on the surface of their series of sharp-edged delta wings tested at zero sideslip, e.g. on the tips of a 76-deg delta wing at $\alpha = 35$ deg. The latter test condition approaches the present one, keeping in mind that the effective sweep of the leeward leading edge of the present delta wing amounts 70 deg at $\beta = 5$ deg. The whorl is suggested to be caused by a separation of the secondary vortex, as sketched in Fig. 28 reproduced from [21]. To the author's knowledge, there exists no experimental evidence of this type of separation. Flowfield surveys could help verify it's existence. Earnshaw and Lawford further observed that the whorl moved towards the apex with increasing α. The present tests indicate that this is not the case if sideslip is involved; the whorl does not displace much when β increases from 4 to 8 deg, and disappears at larger β.

At other test conditions or delta wing geometries, the secondary-separation lines may be located further inboard of the leading edge. At such conditions an outboard shift of the separation lines can be observed downstream of the burst [7]. This shift is caused by the expanding turbulent wake downstream of the burst. Such a shift of the secondary-separation lines was not observed at the present test conditions.

Beyond $\beta = 16$ deg, the distance between the separation line and the leeward leading-edge of the present wing becomes very small. It is therefore believed that a secondary vortex is no longer formed at the larger sideslip angles.

Another phenomenon is the reversal of the skin-friction lines on the windward side. This is visible on the rear part of the wing at $\beta = 5$ deg. On the front part a vortex-induced type of streamline pattern is visible. The reversed flow is associated with the bluff-body type of wake flow downstream of the burst. Between the two regions a node of separation is conjectured to occur on the secondary-separation line. The region affected by reversed flow extends upstream with increasing β. At $\beta = 10$ deg, most of the flow on the windward side is reversed. On the front part of the wing, a region of weak circulating shear flow is visible which is conjectured to originate from a focus of attachment.

The pictures of Fig. 24 do not show much variation in the flow when the sideslip angle increases from 10 to 20 deg. The conjectured topology at the largest β is given in Fig. 27. Compared to the pattern at $\beta = 10$ deg, the focus of attachment is located more

downstream and closer to the leeward edge. Associated with this is a displacement of the attachment line into the leeward direction.

As far as the off-surface flow is concerned, up to $\beta = 8$ deg the flow over the delta wing is dominated by two primary and secondary vortices. The leeward vortices reduce in size, while moving towards the leeward edge with increasing sideslip. The leeward secondary vortex is believed to strongly reduce in size when β is over 8 deg and to have vanished completely when β is larger than 16 deg. Beyond $\beta = 8$ or 10 deg, the flow over the other part of the wing is supposed to be dominated by a large turbulent bubble-type of flow that originates from the focus on the front part of the wing. Much more evidence on the complex topology of the flow over the delta wing in sideslip could be obtained from flowfield surveys that provide vorticity and pressure data.

6.3 Surface-Pressure Measurements

Distributions of the static-pressure coefficient C_p on the upper surface of the wing are shown for several β in Figs. 29 to 34. Apart from Fig. 30, the upper plots show the distributions of C_p at 10 spanwise stations, from $x/c = 0.10$ to 0.99. The bottom plots give a three-dimensional presentation of the distributions at all 15 spanwise stations on the wing upper surface. The C_p-curves in the latter plots have been drawn up to the leading edges ($y/s = +/-1.0$). The value of C_p at these edges was calculated from the measured data by cubic extrapolation. Note that instead of β, the symbol AoS is used in the plots.

At $\beta = 0$ deg, the magnitude of negative C_p or suction induced by the primary vortices is largest at $x/c = 0.10$. The shape of the C_p-curve at this station suggests a strong suction induced by the more outboard located secondary and tertiary vortices. This is the case if the boundary layer is laminar. From the surface-flow pattern it is known that boundary-layer transition occurs downstream of this station. At $x/c = 0.20$, the shape of the C_p-curve is typically that of a turbulent boundary layer; the suction induced by the primary vortices is much higher than that induced by the secondary vortices. Downstream of this station C_p can be seen to increase gradually towards the trailing edge. Only at $x/c = 0.99$ a decrease can be noted at the center of the wing. Up to $x/c = 0.40$, the shape of the C_p-curves gives evidence of a strong primary vortex, while downstream of this station the curves are less steep and smoother. The latter is due to the fact that the vortex core becomes turbulent and extends in the radial direction downstream of the burst at x/c = 0.20. This effect of burst on the pressure distribution was noted earlier in Fig. 12.
When the delta wing is yawed to $\beta = 2$ deg, the suction peaks shifts slightly into the leeward direction. On the leeward side a reduction of the suction occurs at $x/c = 0.10$, while downstream of the latter station the primary suction increases. On the windward side a decrease of the suction occurs, especially, between $x/c = 0.10$ and 0.50. This decrease continues when the wing is yawed to $\beta = 3$ deg. At this angle of sideslip a reduction of the suction can be noted on the leeward side at $x/c = 0.10$ and 0.20, while downstream of these stations the suction continues to increase.
When the delta wing is yawed to $\beta = 5$ deg, the suction peaks continues to shift into the leeward direction. On the leeward side the suction reduces up to $x/c = 0.30$ and increases downstream of this station. The latter may be associated with the downstream

displacement of the burst on this side of the wing. Between the primary suction peak and the leading edge the C_p-curves are flat, giving evidence of the presence of a secondary vortex. On the windward side, a reduction of the suction is evident, especially, at the most upstream stations. This is due to the burst approaching the apex.
When β is increased to 10 deg, the suction peaks continue to shift into the leeward direction. A strong reduction of the suction can be noted on the leeward side upstream of $x/c = 0.60$. The level of C_p at $x/c = 0.10$ and 0.20 has even fallen below that of the more downstream stations. In the surface-streamline pattern a region of circulating flow is observed near the apex. This may cause the strong reduction of the suction on the front leeward side. The level of the C_p-curves on the front of the opposite side reduces also considerably and eventually the curves become flat. The suction on the rear part reduces towards the trailing edge. The value of the integrated upper-surface C_p, or suction force, on the rear part is largest on the windward side.
When β increases to 20 deg, a reduction of the suction and flattening of the curves continues to occur on the front part of the wing. On the rear part, low suction peaks remain visible on the leeward side, indicating that a weak primary vortex is still active on this side. This corresponds with the observations of the surface streamline pattern (Fig. 27). The curves do not show flats induced by a secondary vortex, confirming the suggestion made earlier that at large angles of sideslip a secondary vortex is no longer generated near the leeward edge. The suction force on the leeward side is much lower than that on the opposite side. At $\beta = 20$ deg, the turbulent separated flow on the windward side is responsible for a nearly constant C_p from the apex to the trailing edge.

As far as the location of the suction peaks is concerned, when β increases from 0 to 20 deg, the peaks move gradually outboard from $y/s = 0.65$ to 0.85 on the leeward side of the wing, on the opposite side the peaks move inboard from $y/s = 0.65$ to 0.40.
The effect of β on the C_p-curves on the upper and lower surface at 30%, 50% and 70% chord is shown in Figs. 35 and 36, respectively. As has also been measured by Verhaagen and Naarding [7], the point of largest pressure moves towards the windward leading edge, indicating that the stagnation point moves toward this edge with increasing β.

6.4 Forces and Moments

Plots of force-and-moment data set 1 are given in Figs. 37 to 39. The wing was yawed from -20 to +20 deg, and back again to -20 deg, in steps of 1 deg. The difference between the runs with increasing β (open symbols) and decreasing β (solid symbols) gives an indication of the amount of hysteresis.

The bottom plot of Fig. 37 shows that sideslip has little effect on the tangential-force coefficient C_T (circles) and a small effect on the lateral-force coefficient C_Y (quadrangles). The latter coefficient increases constantly in magnitude with β. The top plot gives evidence that sideslip has a large effect on the normal-force coefficient C_N. The latter coefficient shows an increase when β changes from zero to +/-3 deg. This may be caused by the increase of the suction on the leeward side of the upper surface. At larger angles, the normal force reduces considerably due to the decreasing suction on the wing. Discontinuities and hysteresis loops are visible in the C_N curves. These will be discussed later in this section.

The top plot of Fig. 38 shows that the effect of β on the pitching-moment coefficient C_m is similar to that on C_N. The reduction of C_m when β becomes larger than 3 deg is caused by the reduction of the suction on the front part of the wing upper surface. The effect on the x-coordinate x_p of the center of pressure is shown in the upper plot of Fig. 40. Up to $\beta = 3$ deg, there is an slight upstream displacement of the pressure point, while beyond that angle this point moves into the opposite direction.

The bottom plot of Fig. 38 indicates that the rolling-moment coefficient C_l has a negative gradient between β = -2 and +2 deg, a positive gradient when β increases to 4 deg and a negative gradient again at the larger angles. The latter is due to the decreasing suction force on leeward side of the upper surface. The level of the C_l-curves is lower than would be expected. Theoretically, C_l should be equal to zero at $\beta = 0$ deg. That this is not the case in the present experiment may be due to a small asymmetry in the geometry of the model. This has also an effect on the lateral coordinate y_p of the center of pressure, shown in the bottom plot of Fig. 40, non-dimensionalized by wing span. At zero sideslip, the normal force attaches at $y_p/b = .008$, which is about 5 mm off the wing centerline. The lateral displacement y_p is small between β = -6 and +6 deg. The center of pressure moves into the windward direction at larger β. Fig. 41 illustrates the displacement of the center of pressure over the upper surface of the wing with sideslip. Note that the wing contour has been plotted up to x/c = 0.60.

The curves for the yawing-moment coefficient C_n (Fig. 39) show a small negative gradient at small β. The gradient becomes positive beyond $\beta = 6$ deg.

Discontinuities and hysteresis loops are evident in the curves of the largest coefficients, C_N and C_m. Fig. 42 shows the two C_N-curves from data set 2, Fig. 43 shows the curves separately. When one follows the curves in the direction of yaw, at least 5 regions can be distinguished:

Region	$\lvert\beta\rvert$ **Range (deg)**
1	$10 < \lvert\beta\rvert < 20$
2	$6 < \lvert\beta\rvert < 10$
3	2 or $3 < \lvert\beta\rvert < 6$
4	$\lvert\beta\rvert < 2$ or 3
5	2 or $3 < \lvert\beta\rvert <$ 13 or 17

In region 1, there is a gradual increase of C_N with decreasing $|\beta|$. At $|\beta| = 10$ deg, a discontinuity is visible in the curves. In region 2, C_N continues to increase, albeit less strong and stable. The latter may be a consequence of the instabilities observed in the core flow in this region. The curves in region 3 tend to have a steeper gradient than those in the former region. Inside region 4, C_N reduces from a maximum value at it's edge to a local minimum at zero sideslip. Region 5 shows a reduction of C_N with increasing $|\beta|$. A kink can be seen at $|\beta| = 13$ and 17 deg in the curve of increasing and decreasing β, respectively. At this discontinuity, C_N increases abruptly to the level of the curve that is generated when the wing is yawed into the opposite direction (Fig. 42). The level of the C_N-curve between $|\beta| = 10$ and 17 deg hence depends on the direction of yaw of the wing. Smaller hysteresis effects can be noted in the range $|\beta| < 10$ deg. The test results

obtained so far suggest that the topology of the flow changes most in the latter β-range. Figs. 44 and 45 show the separate curves of C_N and C_l for this range, obtained from data set 3. The variation of the data is evident from the plots. In the C_l-curves a dash-dot-dot line marks the presumed theoretical $C_l = 0$ level. The regions that can be distinguished in the C_N-curves have also been marked in the C_l-curves. From the latter curves it appears that region 5 can be subdivided into two regions (2 or $3 < |\beta| < 4$ deg) and ($4 < |\beta| <$ 13 or 17 deg). The two regions are characterized by a difference in slope. Computation of the local force-and-moment coefficients by integrating the surface-pressure data could help explain the difference in the slopes of the C_l-curves.

7 Conclusions and Recommendations

Wind tunnel tests were conducted to generate data on the effect of sideslip on the aerodynamic characteristics of a flat-plate swept 65-deg delta wing. The tests were carried out at an angle of attack of 30 deg, at angles of sideslip up to 20 deg and a Reynolds number of 2.3 million.

Although the angle of attack of the wing was exactly 30 deg at zero airspeed, elastic deformation of the strut and balance system under aerodynamic load increased the angle to a value of 31.4 deg at zero sideslip, and to 30.8 deg at $\beta = 20$ deg. The effect of the deflections on the sideslip angle were small. Tunnel-wall-interference effects are estimated to be responsible for an upflow angle of the order of 5 deg. This means that the effective angle of attack could have been as large as 36 to 37 deg. The magnitude of the angle of sideslip can be expected to also be affected by tunnel-wall effects. Unfortunately, no theory was available to estimate these effects.

At zero sideslip, the flow over the delta wing is dominated by two primary and secondary vortices. Vortex burst occurs at approximately 20% chord. Upstream of the boundary-layer transition region at about 17% chord, the surface-flow pattern gives evidence of the presence of tertiary vortices. The vortices induce strong suction peaks on the front part of the wing.

With sideslip, the vortices were observed to move towards the leeward edge with increasing sideslip. The vortex burst on the windward wing side moves towards the apex, the burst on the other side moves into the opposite direction. Associated with this is a reduction of the suction on upper surface, especially, on the windward side. The amplitude of the oscillation of the burst along the vortex axis increases with the angle of sideslip. Streamwise instabilities of the core flow were prominent between $\beta = 6$ and 12 deg.
The boundary-layer transition region on the windward side moves towards the apex with increasing angle of sideslip. On the leeward side, this region moves into the opposite direction. A whorl is visible near the leeward wing tip at β from 4 to 8 deg. This may be due to a local lift-off of the leeward secondary-vortex from the upper surface. The leeward secondary vortex is believed to strongly reduce in size when β is over 8 deg and to have vanished completely from the wing when β is larger than 16 deg.
From $\beta = 5$ deg a reversal of the streamlines starts to occur on the rear part of the windward side. The region affected by reversed flow extends upstream with increasing sideslip.
From $\beta = 10$ to 20 deg, a region of weak circulating shear flow is visible on the front part of the wing. Downstream of this region, the surface-flow patterns and surface-pressures suggest a vortex-type of flow near the leeward edge and a bubble-type of flow on the remaining upper surface.

The conjectured off-surface flow topologies are complex and suggest that most changes in the flow occur in the range $|\beta| < 10$. To confirm these topologies, it is recommended to have detailed surveys conducted of the flowfield over the delta wing.

Sideslip has a large effect on the normal force, little effect on the tangential force and a small effect on the lateral force. As far as the moments are concerned, sideslip has most effect on the pitching-moment, the effect on the rolling and yawing moment is smaller

and of the same order of magnitude. Discontinuities and hysteresis effects are visible in the force-and-moment curves. At least 5 regions can be distinguished characterized by a difference in slope.

The development of tunnel-wall-interference correction theories that can be applied for vortex-flow-configurations tested at high α and β is strongly encouraged. At such test conditions, the extended viscous wakes generated over the configuration can be expected to have a significant effect on blockage and flow angularity.

8 Acknowledgements

The author thanks Dr. Charles Jobe of WPAFL for the useful discussions and the interesting visits to his research facilities. This study was supported by the Air Force Office of Scientific Research under EOARD contract SPC 97-4067 with Dr. Charbel Raffoul as monitor.

9 References

[1] Huang, X.Z., Hanff, E.S. and Jobe C.E., "Surface Flow Topology on a Delta Wing at High Incidence for a range of Roll Angles," AIAA 96-2398-CP, New Orleans, June 1996

[2] Jenkins, J.E., "Nonlinear Aerodynamic Characteristics of a 65 Degree Delta Wing in Rolling Motion: Implications to Testing and Flight Mechanics Analysis," AIAA 97-0742, Reno, Jan. 1997

[3] Verhaagen N.G., Report Window-on-Science Visit, July 1996

[4] Ericsson L.E., "Effect of Fuselage Geometry on Delta Wing Vortex Breakdown," AIAA 97-0746, Reno, Jan. 1997

[5] Johnson, J.L., Grafton, S.B. and Yip, L.P., "Exploratory Investigation of the Effects of Vortex Bursting on the High Angle-of-Attack Lateral-Direction Stability Characteristics of highly-Swept Wings," AIAA 80-0463, Reno?, 1980

[6] Hoak, D.E., "USAF Stability and Control DATCOM", 1978

[7] Verhaagen N.G. and Naarding S.H.J., "Experimental and Numerical Investigation of the Vortex Flow over a Sideslipping Delta Wing," *Journal of Aircraft*, Vol. 26, 11, Nov. 1989

[8] Verhaagen N.G., Meeder J.P. and Verhelst J.M., "Boundary Layer Effects on the Flow of a Leading Edge Vortex," AIAA 93-3463-CP, Monterey, August 1993

[9] McKernan, J.F. and Nelson, R.C., "An Investigation of the Breakdown of the Leading Edge Vortices on a Delta Wing at High Angles of Attack," AIAA 83-2114, Gatlinburg, August 1983

[10] Verhaagen N.G., "Tunnel Wall Effect on the Flow around a 76/40-deg Double-Delta Wing," AIAA 98-0312, Reno, Jan. 1998

[11] Hsing, C-C.A. and Lan, C.E., "Low-Speed Wall Interference Assessment/Correction with Vortex Flow Effect," *Journal of Aircraft*, Vol. 34, No. 2, March-April 1997, pp. 220-227

[12] Weinberg, Zvi, "Effect of Tunnel Walls on Vortex Breakdown Location over Delta Wings," *AIAA Journal*, Vol. 30, No. 6, June 1992

[13] Lowson, M.V. and Riley, A.J., "Vortex Breakdown Control by Delta Wing Geometry," *Journal of Aircraft*, Vol. 32, No. 4, 1995, pp. 832-838

[14] Pelletier, A. and Nelson, R.C., "Factors Influencing Vortex Breakdown over 70-deg Delta Wings," AIAA-95-3469-CP, 1995

[15] Wentz, W.H. and Kohlman, D.L., "Vortex Breakdown on Slender Sharp-Edged Wings," *Journal of Aircraft*, Vol. 8, No. 3, 1997

[16] Huang, X.Z., Sun, Y.Z. and Hanff E.S., "Further Investigations of Leading-Edge Vortex Breakdown over Delta Wings," AIAA 97-2263-CP, Atlanta, June 1997

[17] Menke, M. and Gursul, I., "Self-Excited Oscillations of Vortex Breakdown Location over Delta Wings," AIAA 97-0744, Reno, Jan. 1997

[18] Mitchell, A., Barberis, D. and Delery, J., "Oscillation of Vortex Breakdown Location and Its Control by Tangential Blowing," AIAA 98-2914, Albuquerque, June 1998

[19] Visser, K.D. and Washburn, A.E., "Transition Behavior on Flat Plate Delta Wings," AIAA 94-1850, Colorado Springs, June 1994

[20] Jobe, C.E., Huang, X.Z. and Jenkins, J.E., "Impact of Static Topological Changes on Dynamic Airloads," AIAA Workshop III: Delta Wings-Unsteady Aerodynamics and Modeling, AIAA Atmospheric Flight Mechanics Conference, Aug. 1995.

[21] Earnshaw, P.B. and Lawford, J.A., "Low-Speed Wind-Tunnel Experiments on a Series of Sharp-Edged Delta Wings," Aeronautical Research Council, R. & M. No. 3424, 1966

10 Tables

Table 1. Distribution of taps on upper surface

x/c	y/s x 100																
x 100	0	10	20	30	40	45	50	55	60	65	70	75	80	85	90	95	99
10	⊙	⊙	⊙	⊙	⊙	⊙	⊙	⊙	⊙	⊙	⊙	⊙	⊙	⊙			
20	⊙	⊙	⊙	⊙	⊙	⊙	⊙	⊙	⊙	⊙	⊙	⊙	⊙	⊙	⊙		
30	⊙	⊙	⊙	⊙	⊙	⊙	⊙	⊙	⊙	⊙	⊙	⊙	⊙	⊙	⊙	⊙	
40	⊙	⊙	⊙	⊙	⊙	⊙	⊙	⊙	⊙	⊙	⊙	⊙	⊙	⊙	⊙	⊙	
50	⊙	⊙	⊙	⊙	⊙	⊙	⊙	⊙	⊙	⊙	⊙	⊙	⊙	⊙	⊙	⊙	
55	⊙	⊙	⊙	⊙	⊙	⊙	⊙	⊙	⊙	⊙	⊙	⊙	⊙	⊙	⊙	⊙	
60	⊙	⊙	⊙	⊙	⊙	⊙	⊙	⊙	⊙	⊙	⊙	⊙	⊙	⊙	⊙	⊙	
65	⊙	⊙	⊙	⊙	⊙	⊙	⊙	⊙	⊙	⊙	⊙	⊙	⊙	⊙	⊙	⊙	
70	⊙	⊙	⊙	⊙	⊙	⊙	⊙	⊙	⊙	⊙	⊙	⊙	⊙	⊙	⊙	⊙	
75			⊙	⊙	⊙	⊙	⊙	⊙	⊙	⊙	⊙	⊙	⊙	⊙	⊙	⊙	
80			⊙	⊙	⊙	⊙	⊙	⊙	⊙	⊙	⊙	⊙	⊙	⊙	⊙	⊙	
85	⊙	⊙	⊙	⊙	⊙	⊙	⊙	⊙	⊙	⊙	⊙	⊙	⊙	⊙	⊙	⊙	⊙
90	⊙	⊙	⊙	⊙	⊙	⊙	⊙	⊙	⊙	⊙	⊙	⊙	⊙	⊙	⊙	⊙	⊙
95	⊙	⊙	⊙	⊙	⊙	⊙	⊙	⊙	⊙	⊙	⊙	⊙	⊙	⊙	⊙	⊙	⊙
99	⊙	⊙	⊙	⊙	⊙	⊙	⊙	⊙	⊙	⊙	⊙	⊙	⊙	⊙	⊙	⊙	⊙

Table 2. Distribution of taps on under surface

x/c	y/s x 100																
x 100	0	10	20	30	40	45	50	55	60	65	70	75	80	85	90	95	99
30	⊙		⊙		⊙		⊙	⊙									
50	⊙		⊙		⊙		⊙	⊙	⊙	⊙	⊙						
70	⊙		⊙		⊙		⊙	⊙	⊙	⊙	⊙	⊙	⊙				

11 Figures

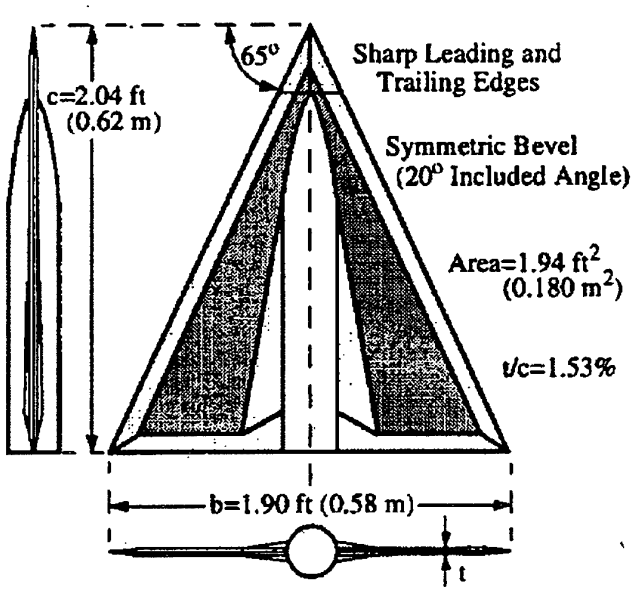

Figure 1: AFRL wing geometry

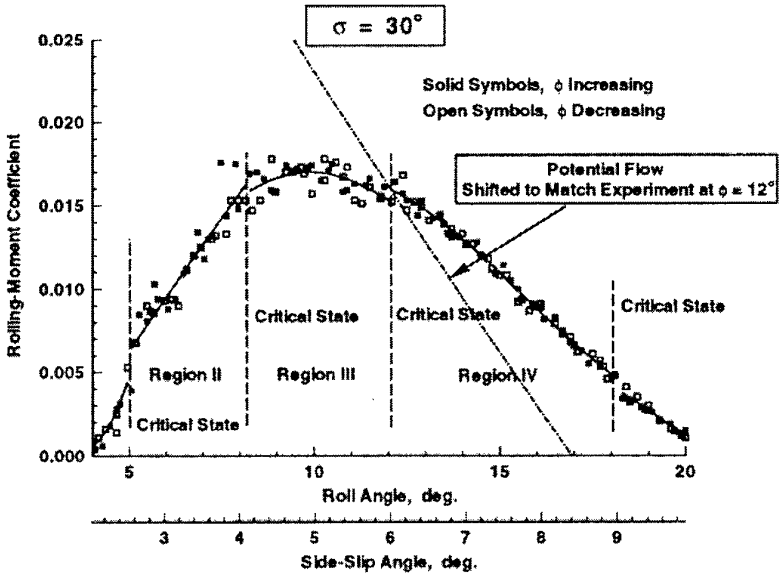

Figure 2: Effect of ϕ on rolling-moment coefficient

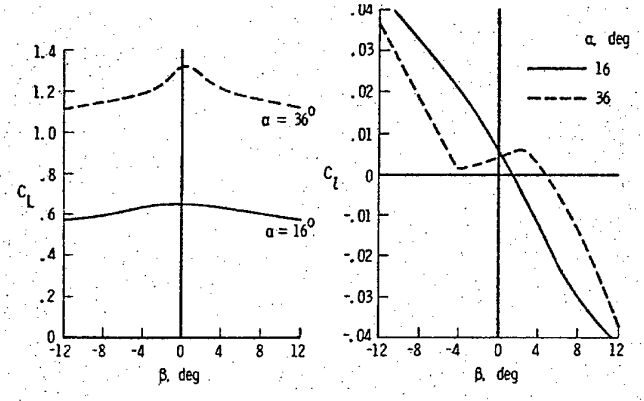

Figure 3: Effect of β on lift and rolling-moment coefficient of a 70-deg delta wing at low and high α (Johnson, et al [5])

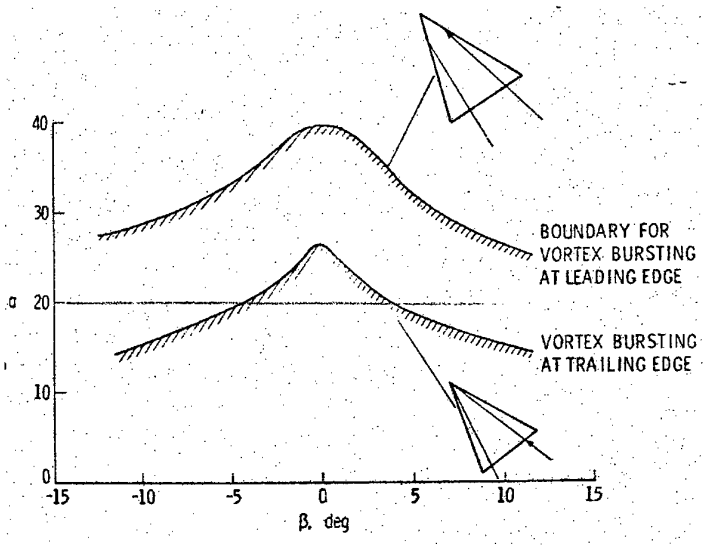

Figure 4: Boundaries for vortex burst at the leading- and trailing-edge on the windward side of a 70-deg delta wing (Johnson, et al [5])

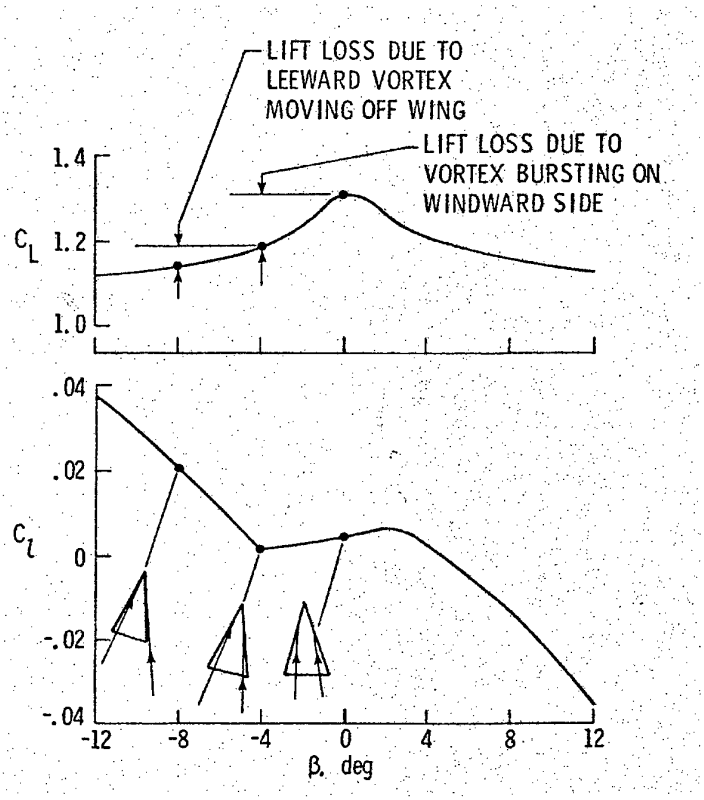

Figure 5: Effect of β on lift and rolling-moment coefficient of a 70-deg delta wing at $\alpha = 36$ deg (Johnson, et al [5])

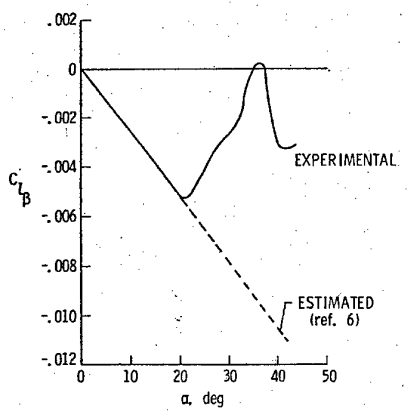

Figure 6: Comparison of measured and estimated values of C_{l_β} for a 70-deg delta wing (Johnson, et al [5])

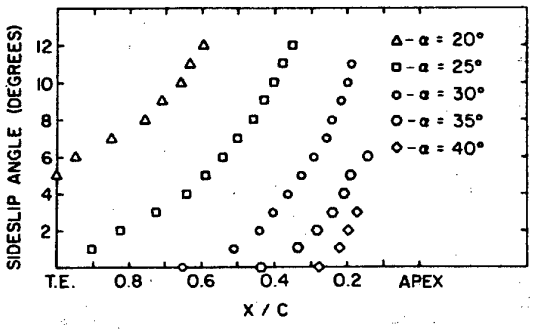

Figure 7: Effect of β on windward vortex burst location of a 70-deg delta wing (McKernan and Nelson [9])

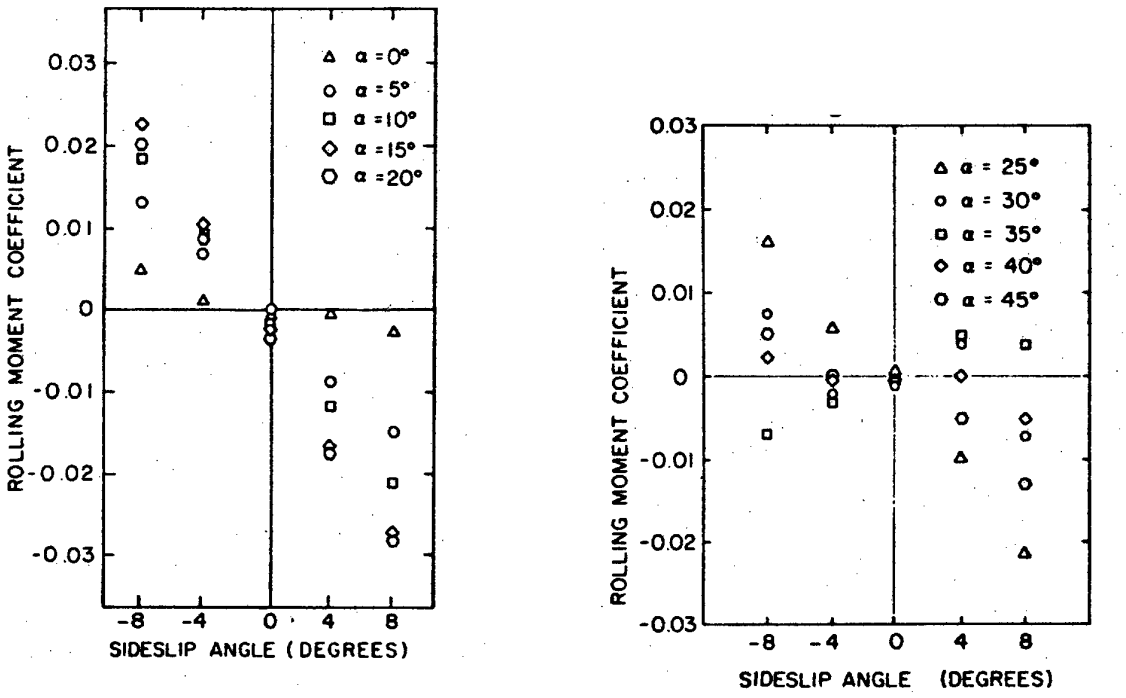

a. α = 0-20 deg

b. α = 25-45 deg

Figure 8: Effect of β on rolling-moment coefficient of a 70-deg delta wing at various α (McKernan and Nelson [9])

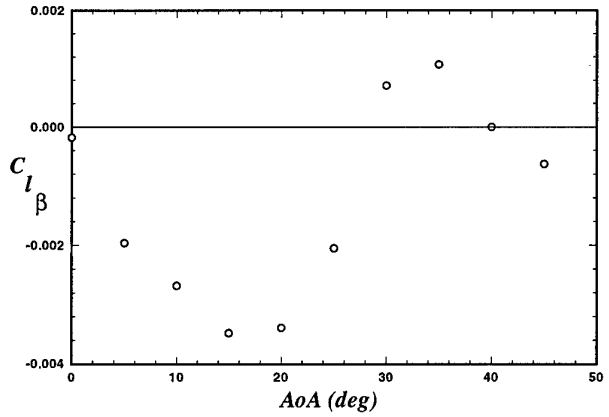

Figure 9: Effect of α on C_{l_β} of the 70-deg delta wing tested by McKernan and Nelson [9]

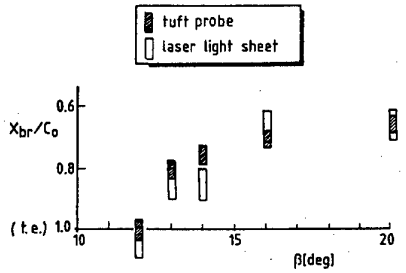

Figure 10: Burst location on windward side of a 76-deg delta wing at $\alpha =$ 21 deg (Verhaagen and Naarding [7])

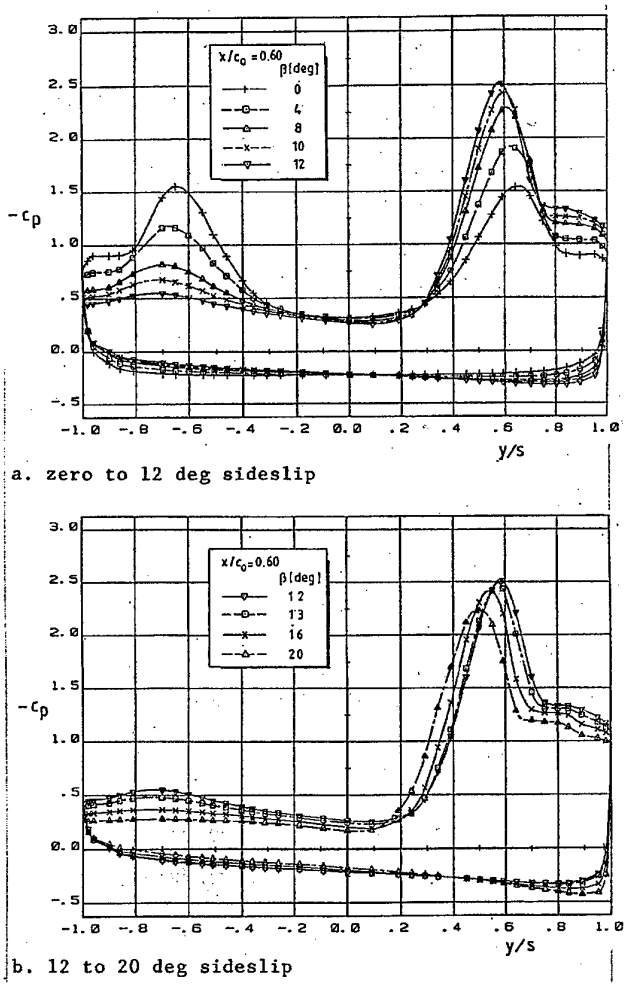

Figure 11: Effect of β on spanwise pressure distribution of a 76-deg delta wing at $\alpha = 21$ deg (Verhaagen and Naarding [7])

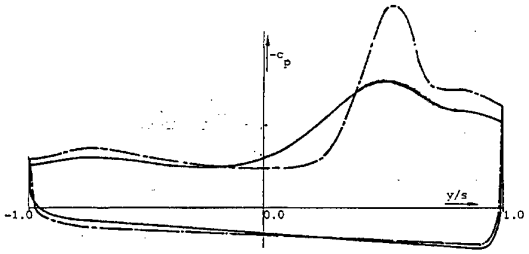

Figure 12: Effect of burst on spanwise pressure distribution near trailing edge of a 76-deg delta wing at $\alpha = 21$ deg (Verhaagen and Naarding [7]); the dashed line represents the C_p-curve upstream, the solid line downstream of the burst location.

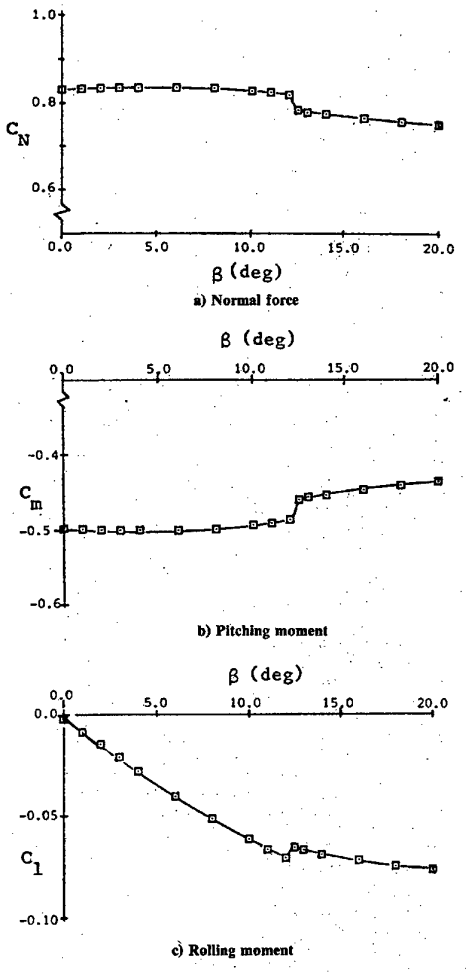

Figure 13: Effect of β on force-and-moment coefficients of a 76-deg delta wing at $\alpha = 21$ deg (Verhaagen and Naarding [7])

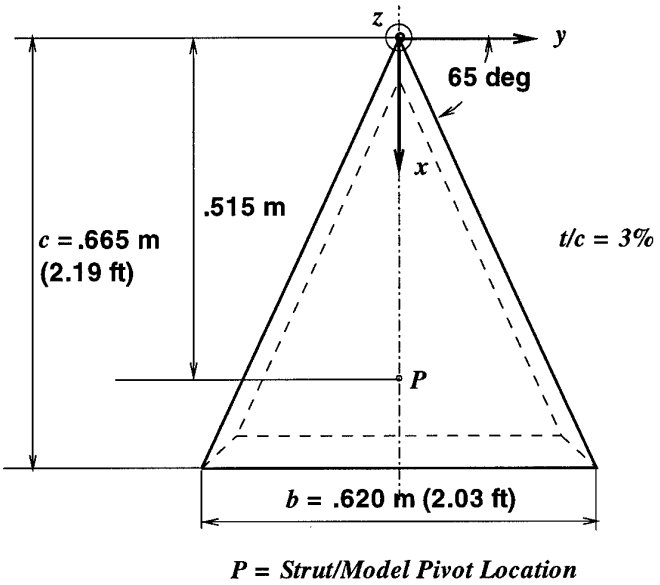

Figure 14: TUD wing geometry

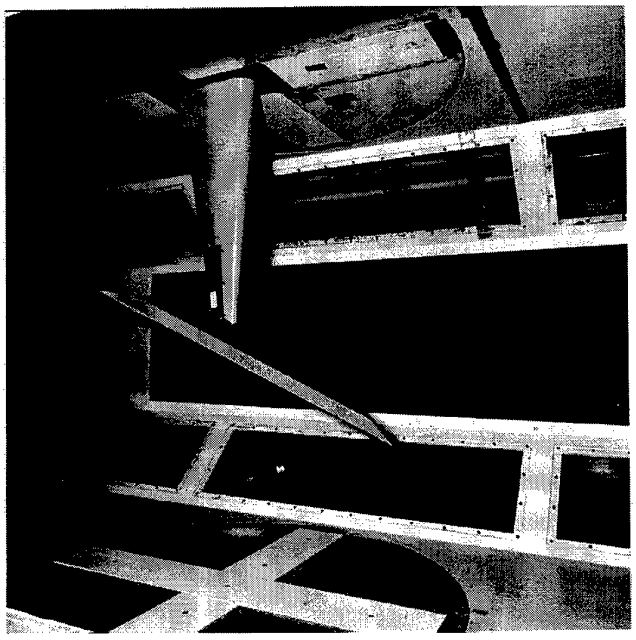

Figure 15: Delta wing in LTT

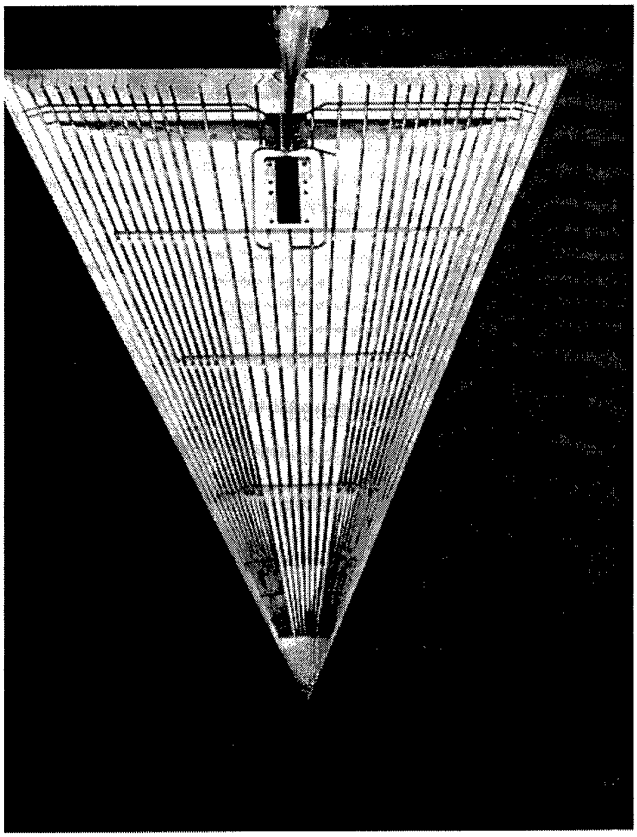

Figure 16: Delta wing used for surface-pressure measurements

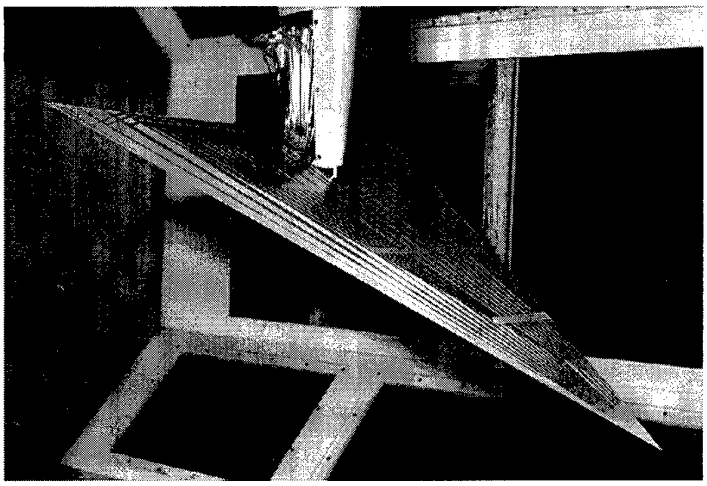

Figure 17: Delta wing with pressure taps in LTT

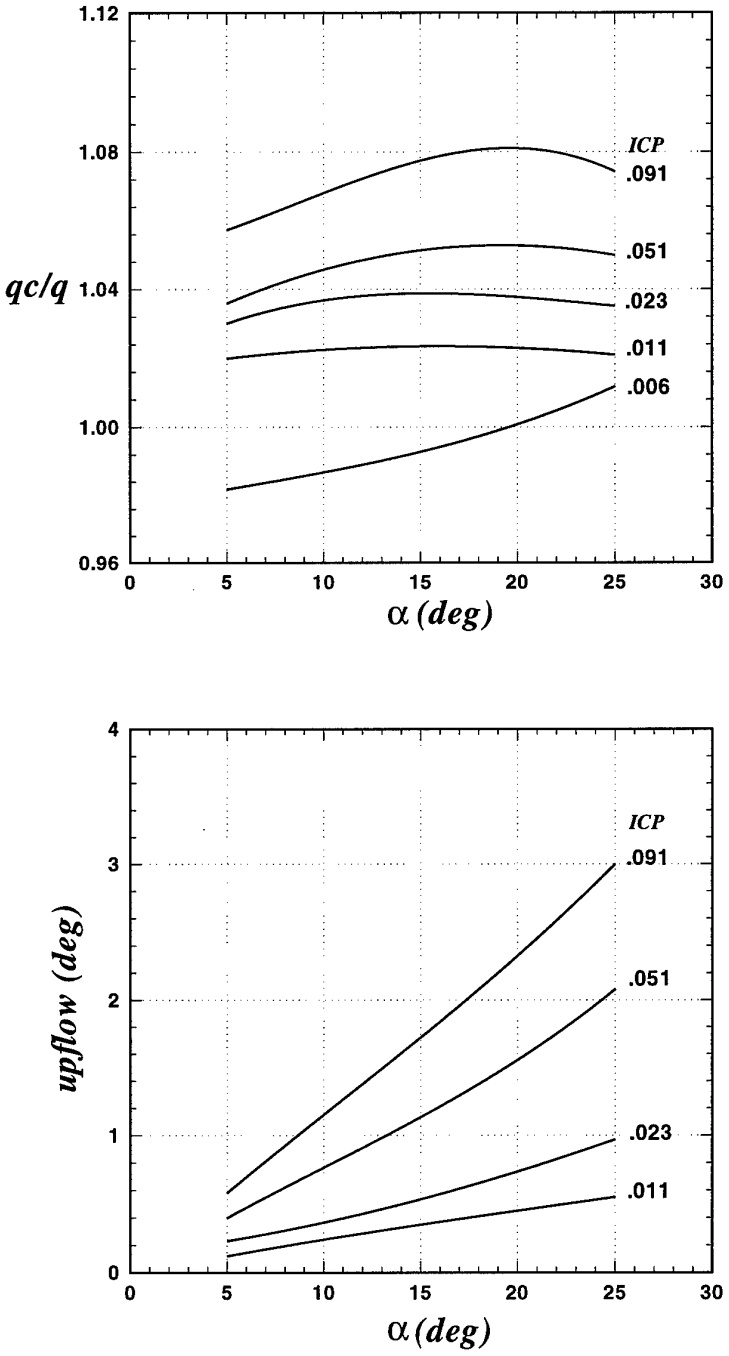

Figure 18: Effect of α on blockage and upflow corrections of a general wing-body/strake configuration (Hsing & Lan [11])

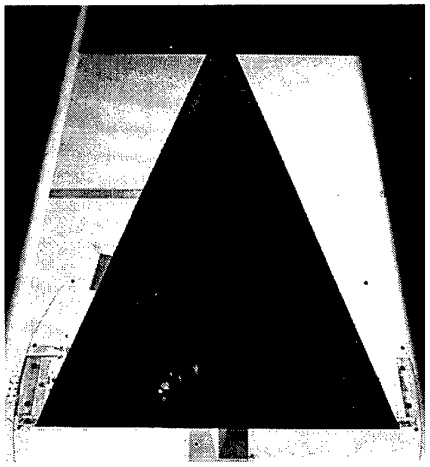

$\beta = 0$ deg

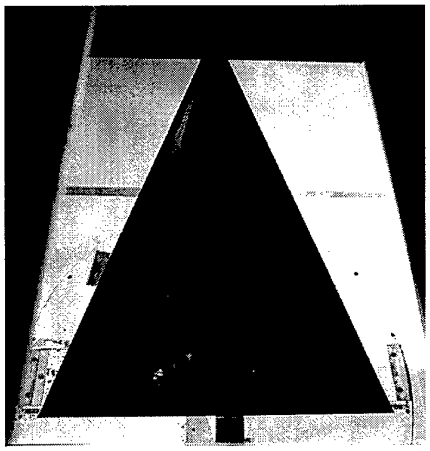

$\beta = 2$ deg

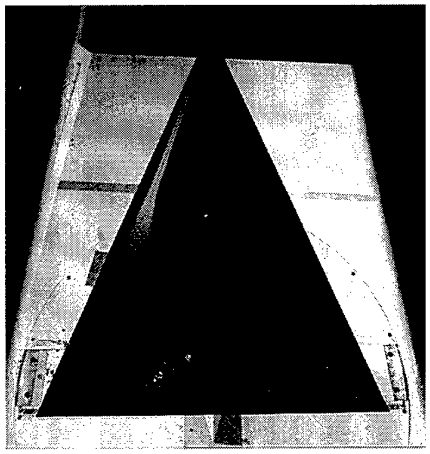

$\beta = 4$ deg

Figure 19: Condensed vortex cores

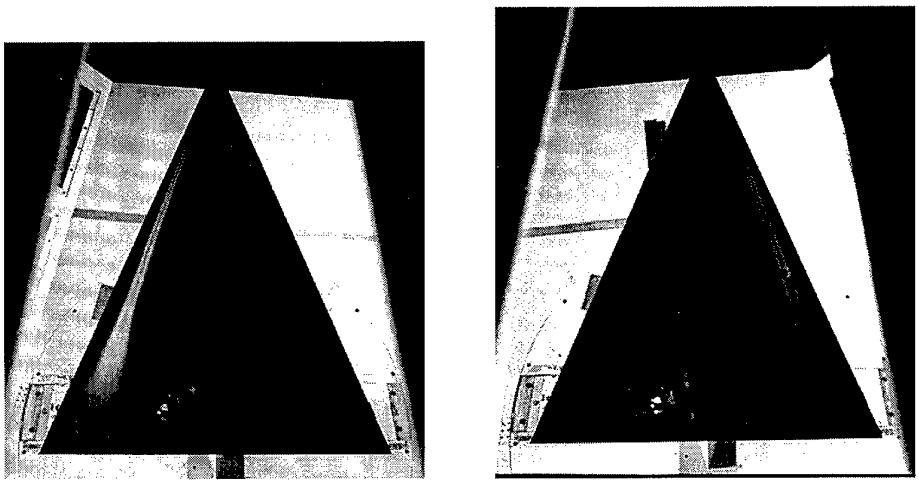

β = +6 deg β = -6 deg

Figure 20: Condensed vortex cores

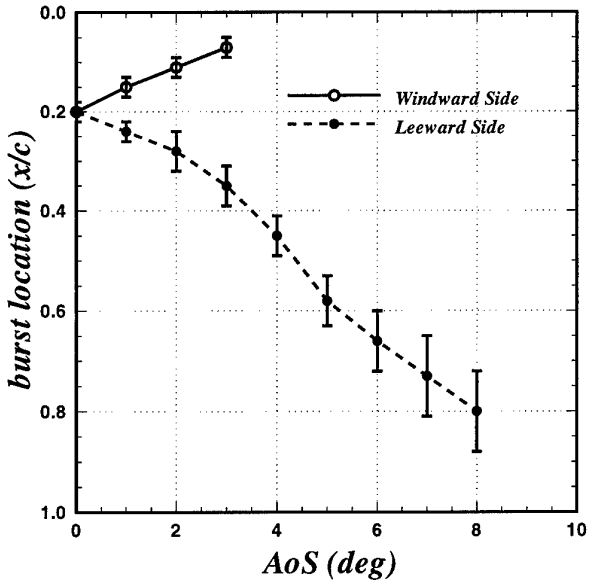

Figure 21: Effect of β on bursting location

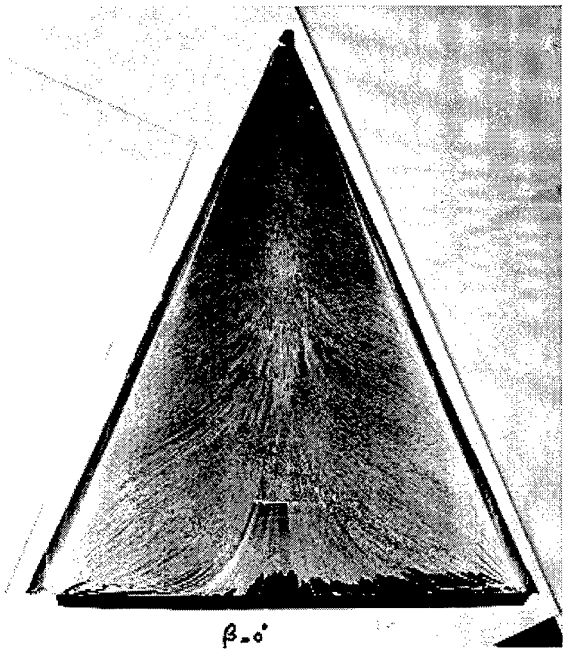

$\beta = 0$ deg

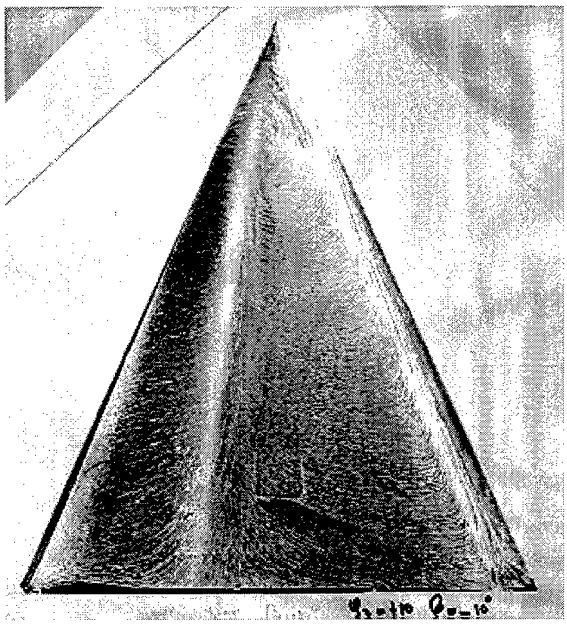

$\beta = 10$ deg

Figure 22: Upper-surface flow pattern visualized using oilflow

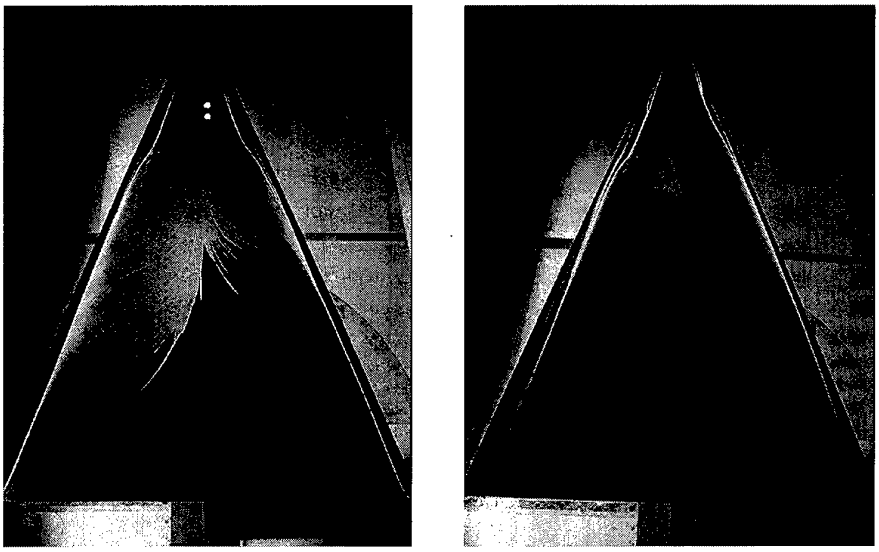

$\beta = 1$ deg (left-hand), and 3 deg (right-hand picture)

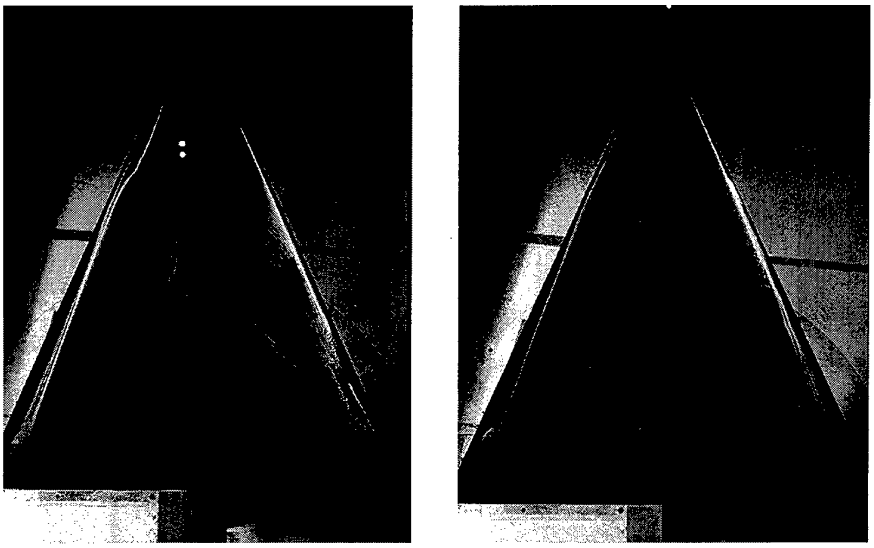

$\beta = 5$ deg (left-hand), and 7 deg (right-hand picture)

Figure 23: Upper-surface flow pattern at different β, as visualized using an oil/fluorescent-dye technique

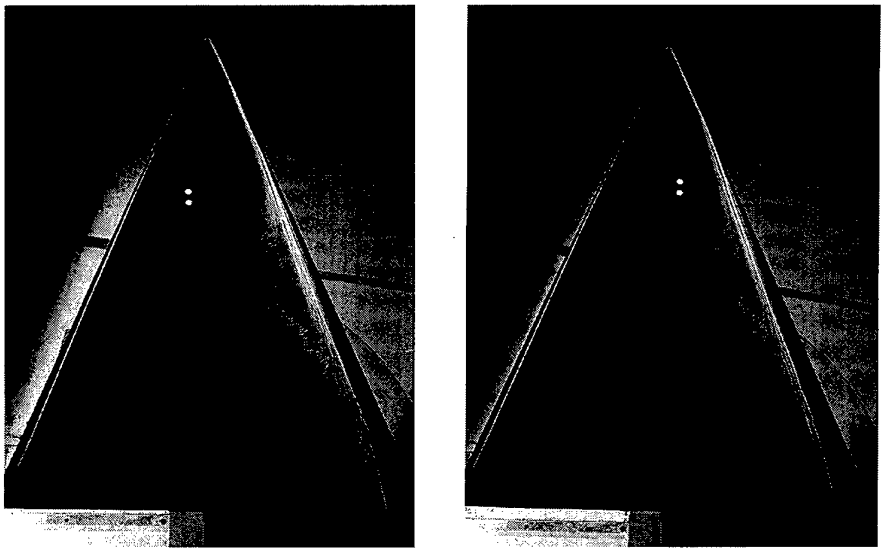

β = 10 deg (left-hand), and 12 deg (right-hand picture)

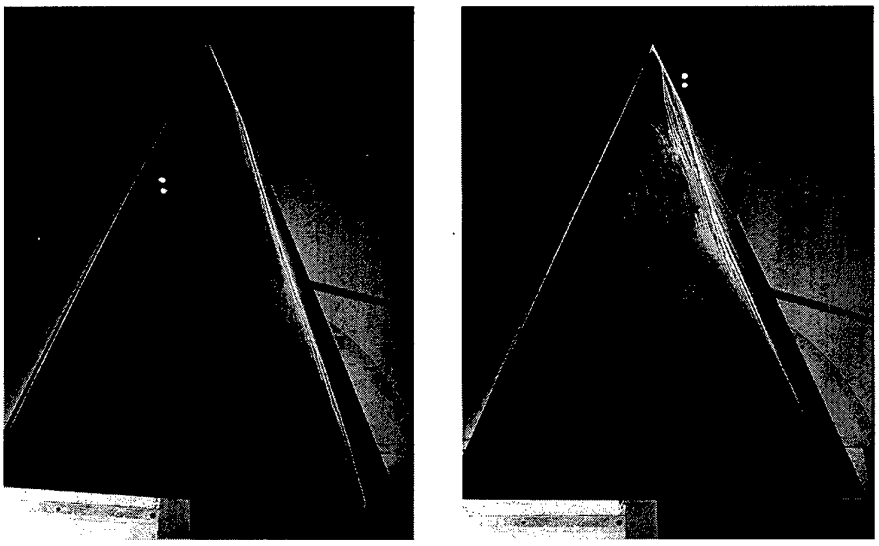

β = 14 deg (left-hand), and 20 deg (right-hand picture)

Figure 24: Upper-surface flow pattern at different β, as visualized using an oil/fluorescent-dye technique (Continued)

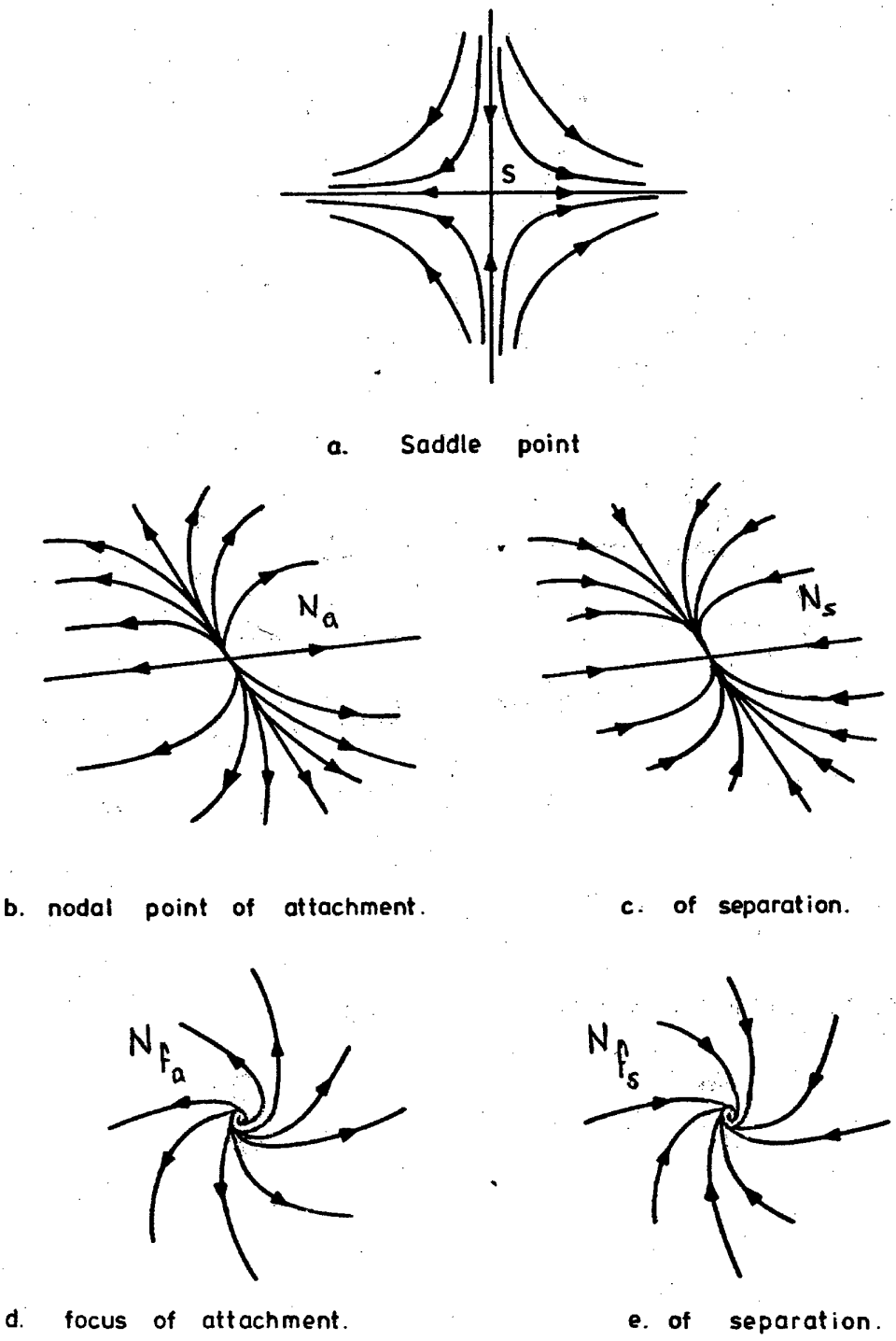

Figure 25: Singular points

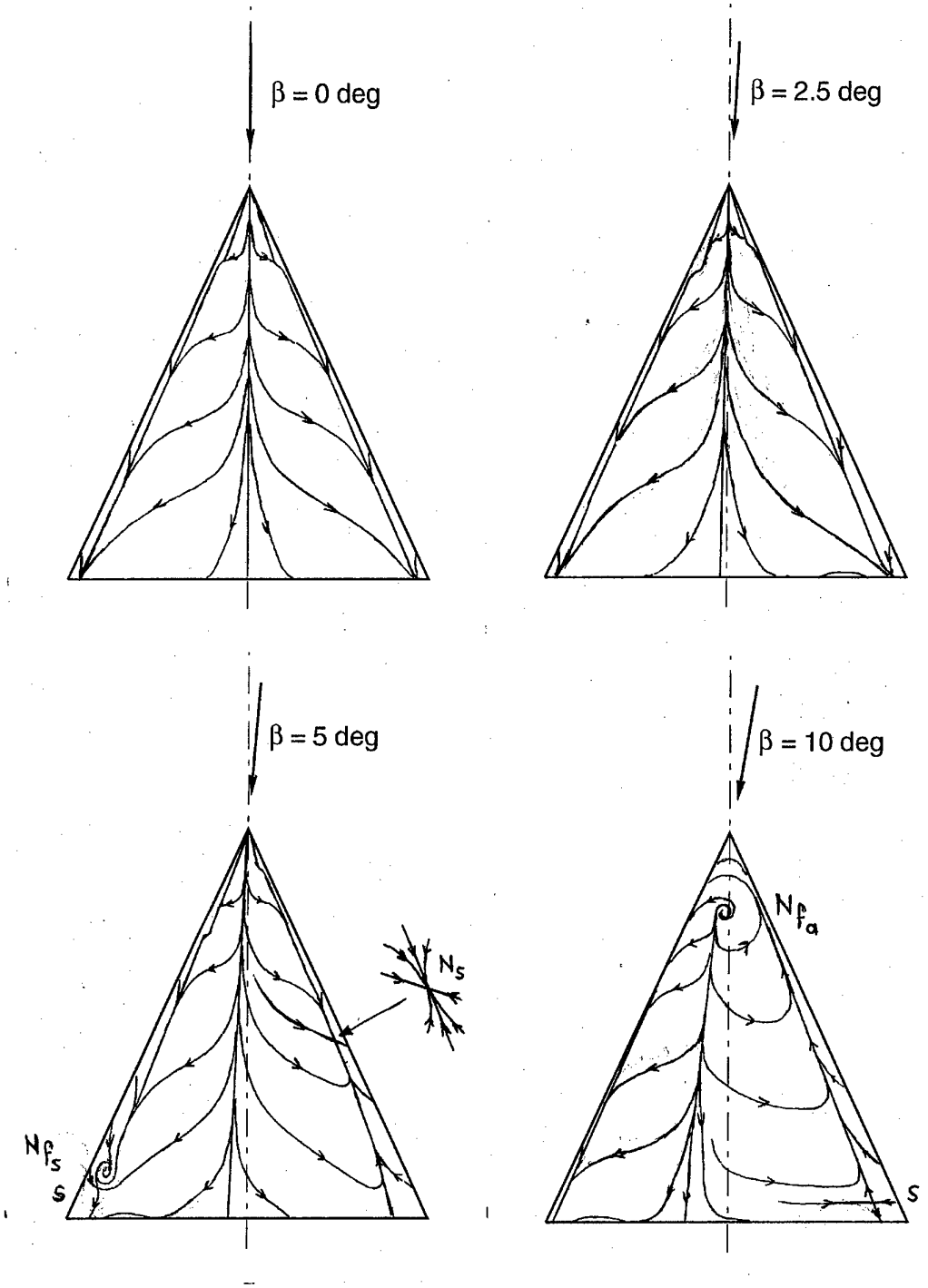

Figure 26: Conjectured topology of upper-surface flow for β up to 10 deg

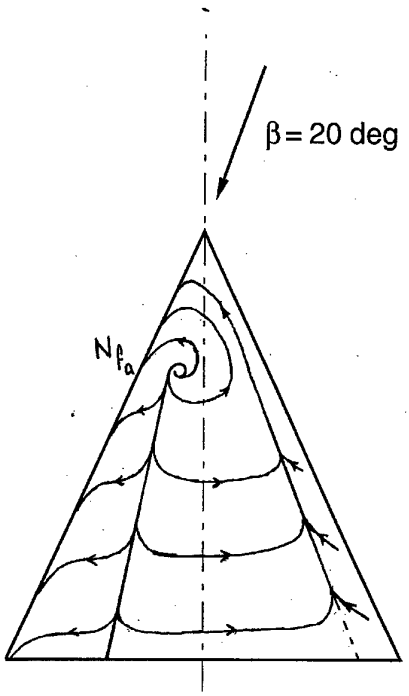

Figure 27: Conjectured topology of flow for β= 20 deg

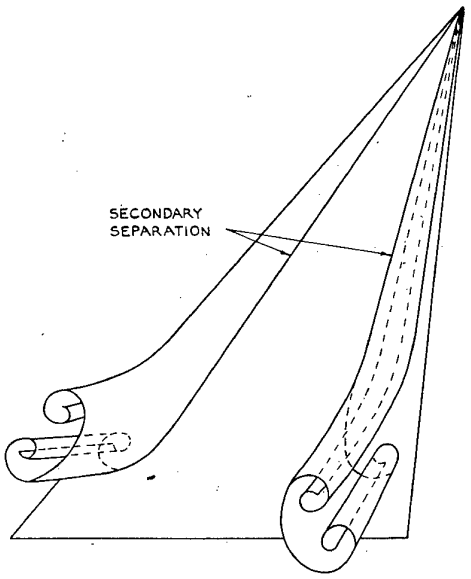

Figure 28: Secondary-vortex system associated with "whorl" surface pattern, as suggested by Earnshaw & Lawford [21]

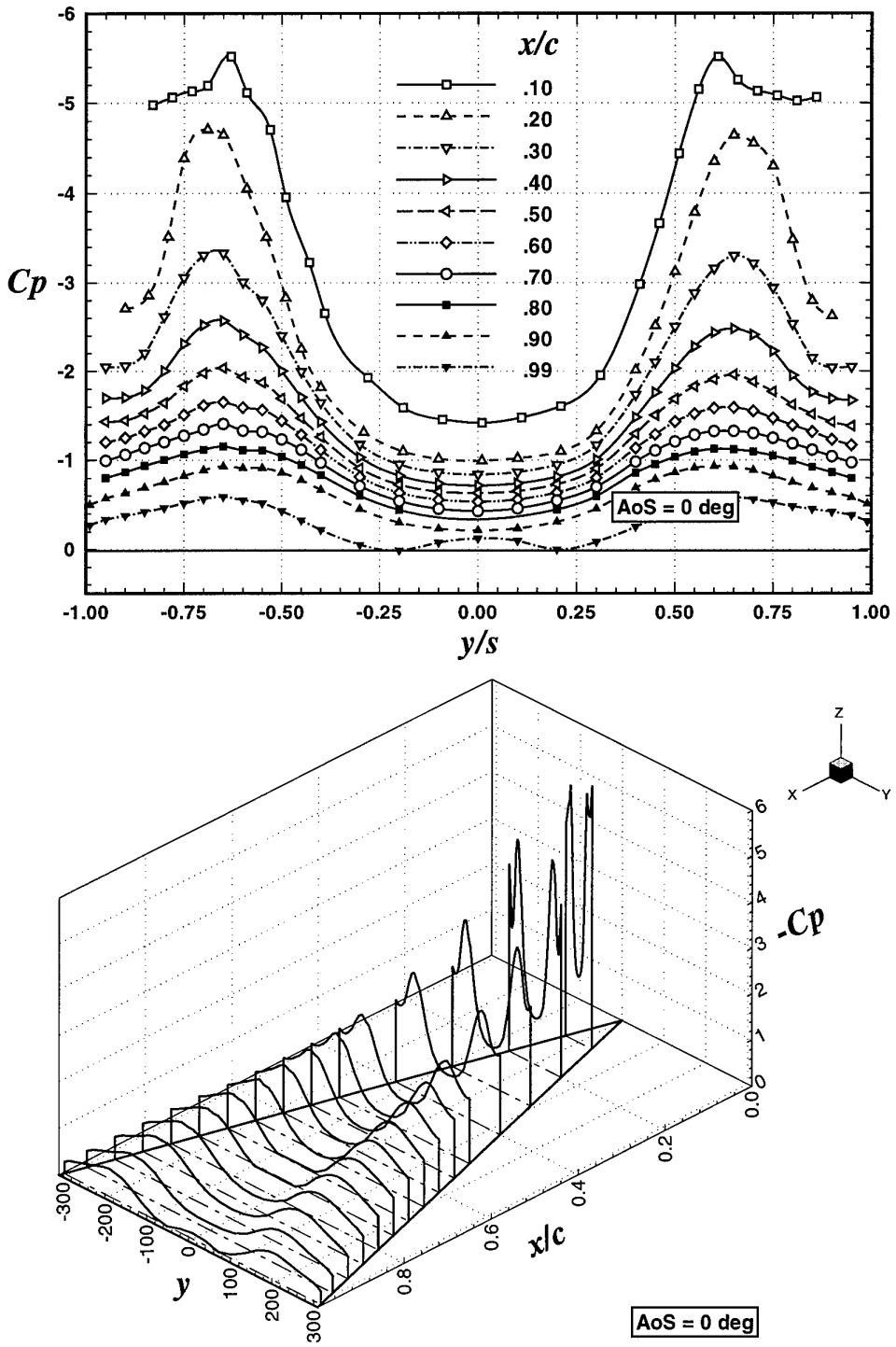

Figure 29: Surface pressure for $\beta = 0$ deg

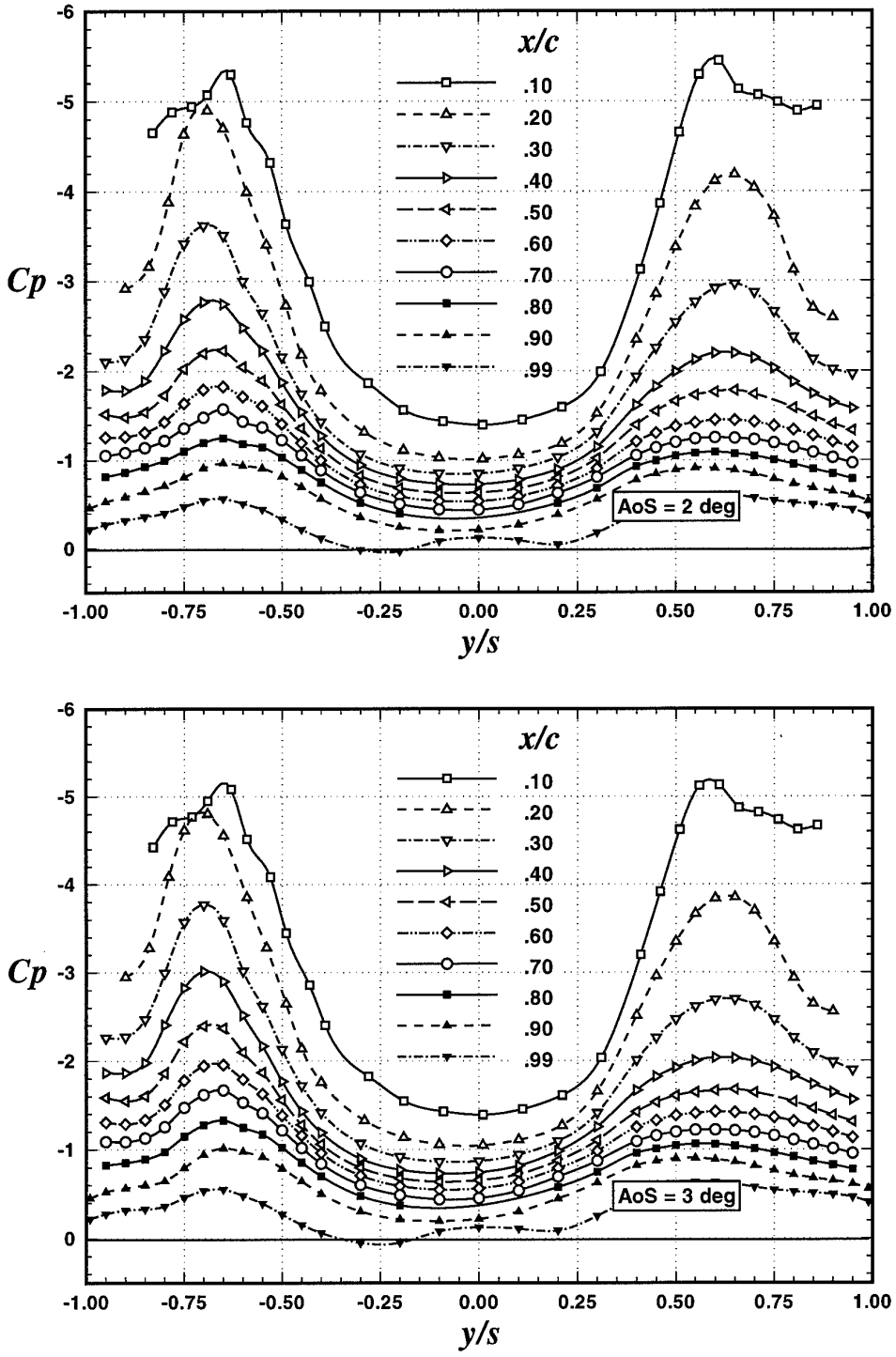

Figure 30: Surface pressure for $\beta = 2$ and 3 deg

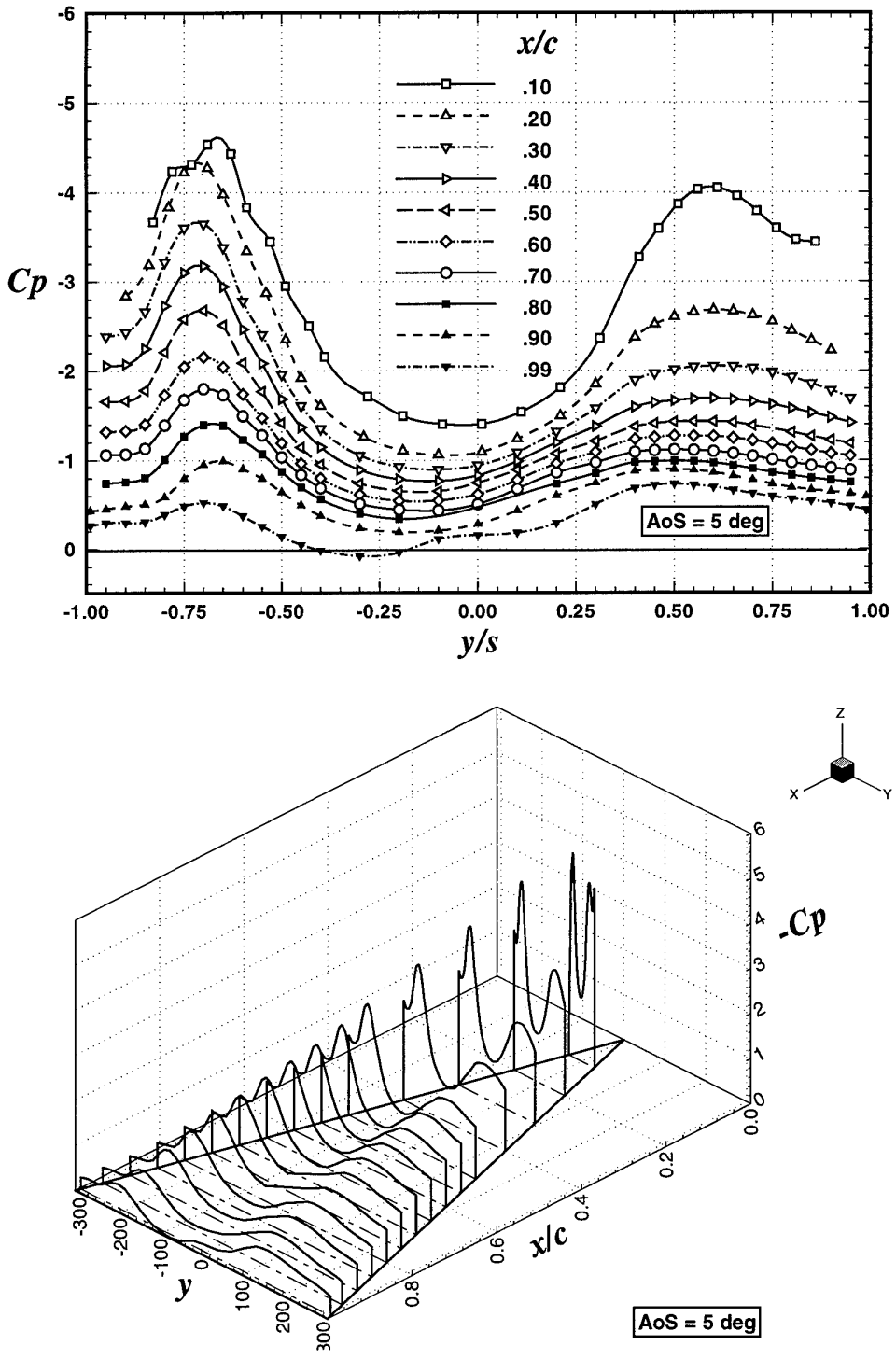

Figure 31: Surface pressure for $\beta = 5$ deg

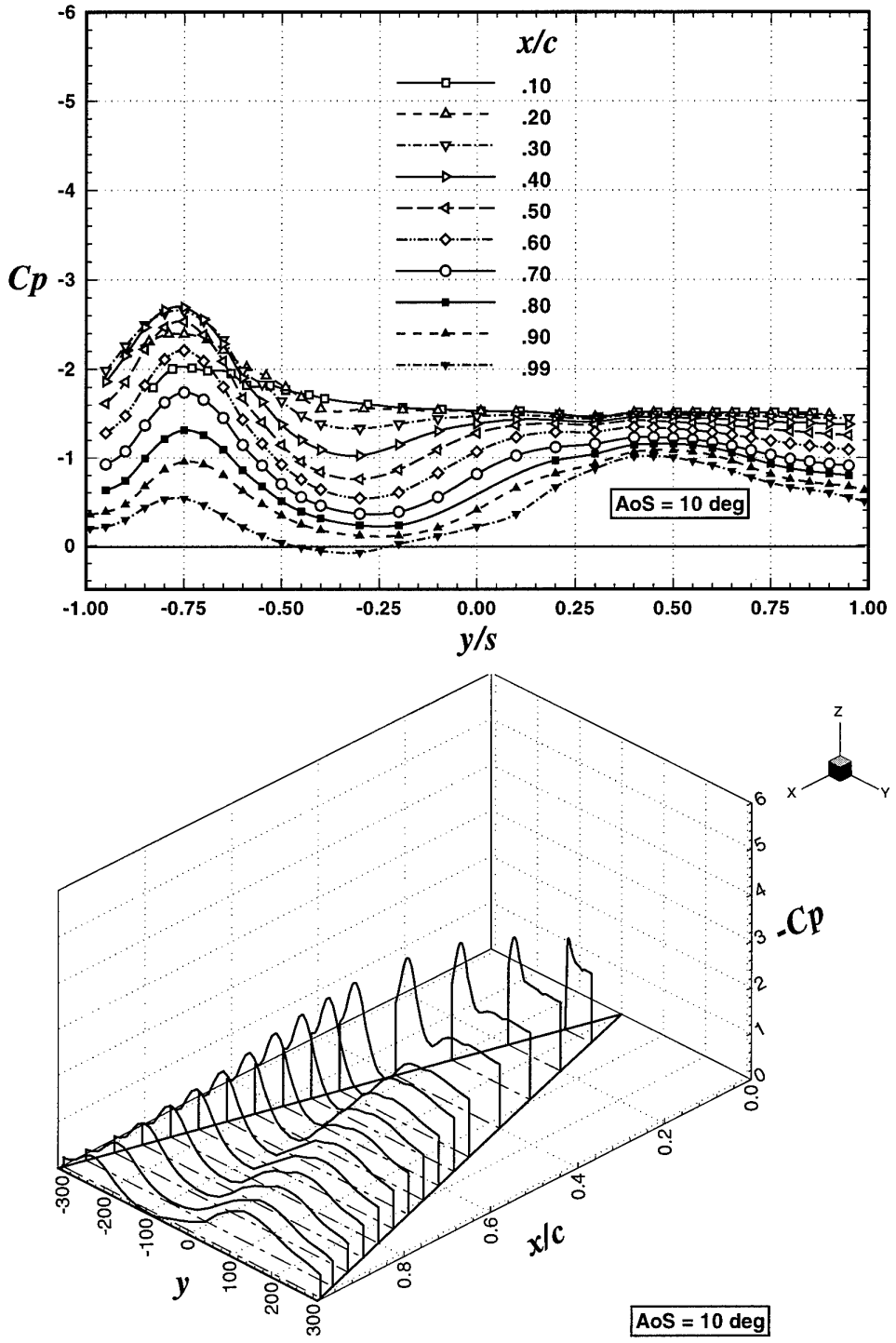

Figure 32: Surface pressure for $\beta = 10$ deg

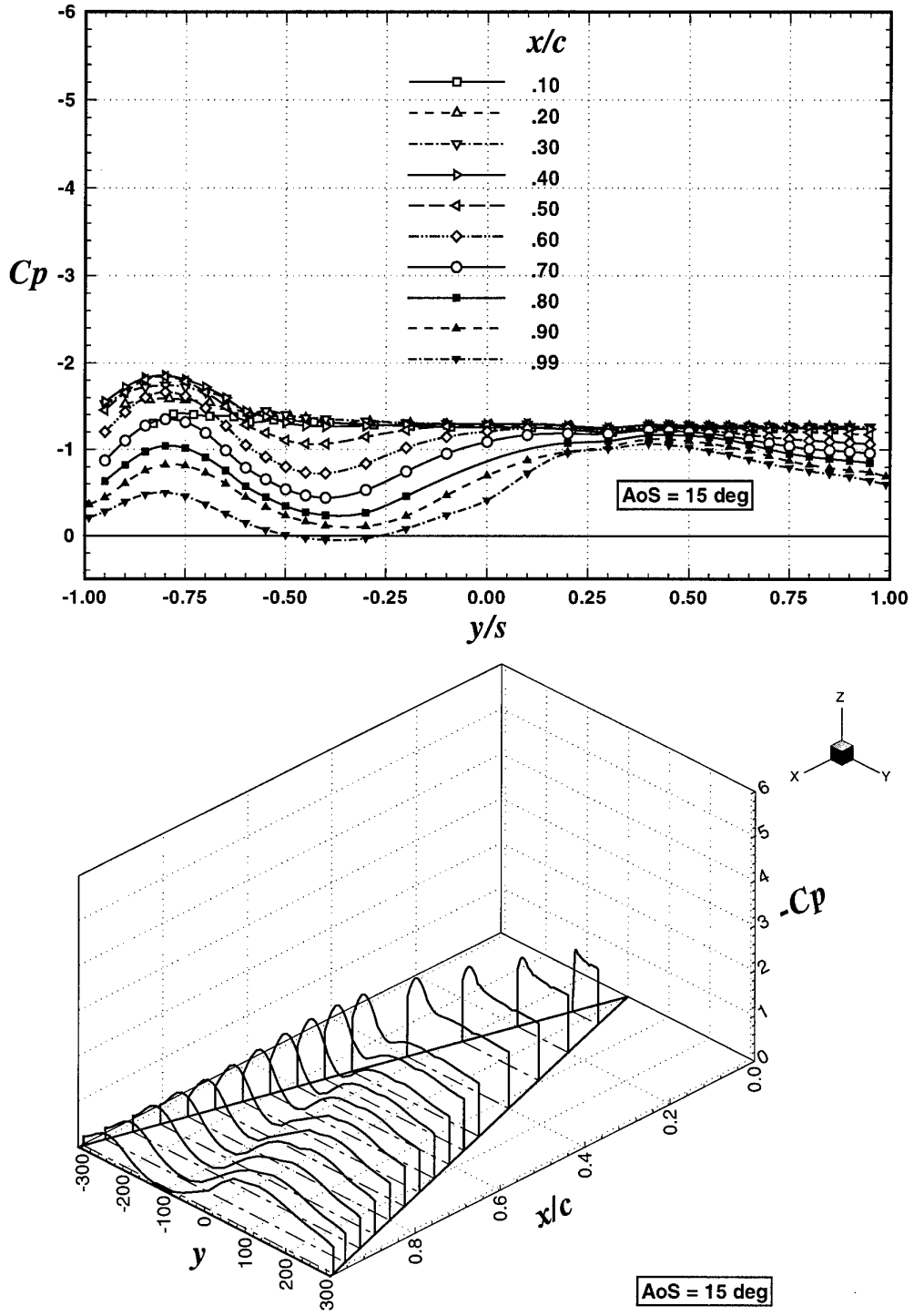

Figure 33: Surface pressure for $\beta = 15$ deg

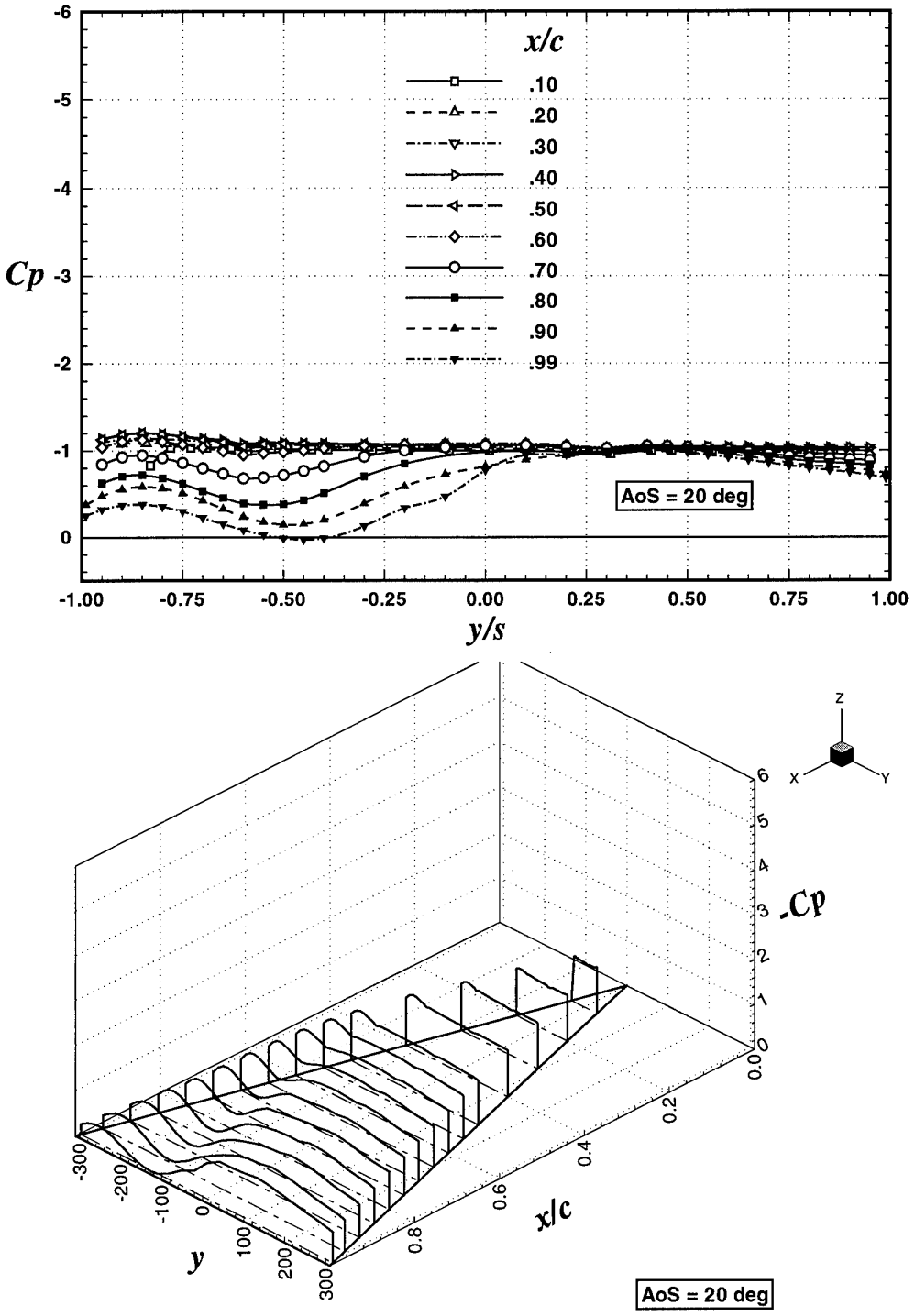

Figure 34: Surface pressure for $\beta = 20$ deg

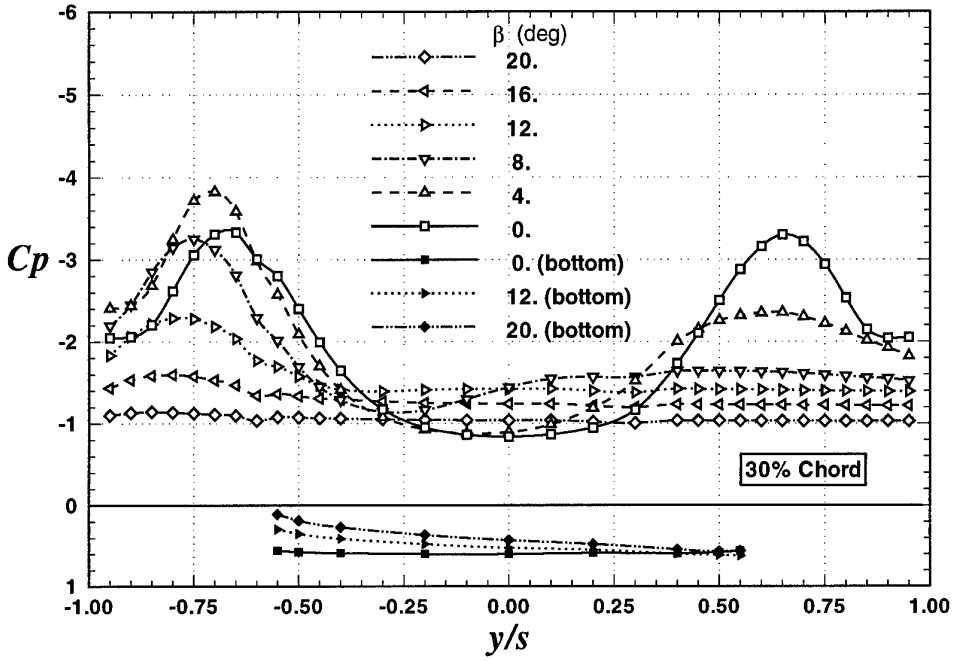

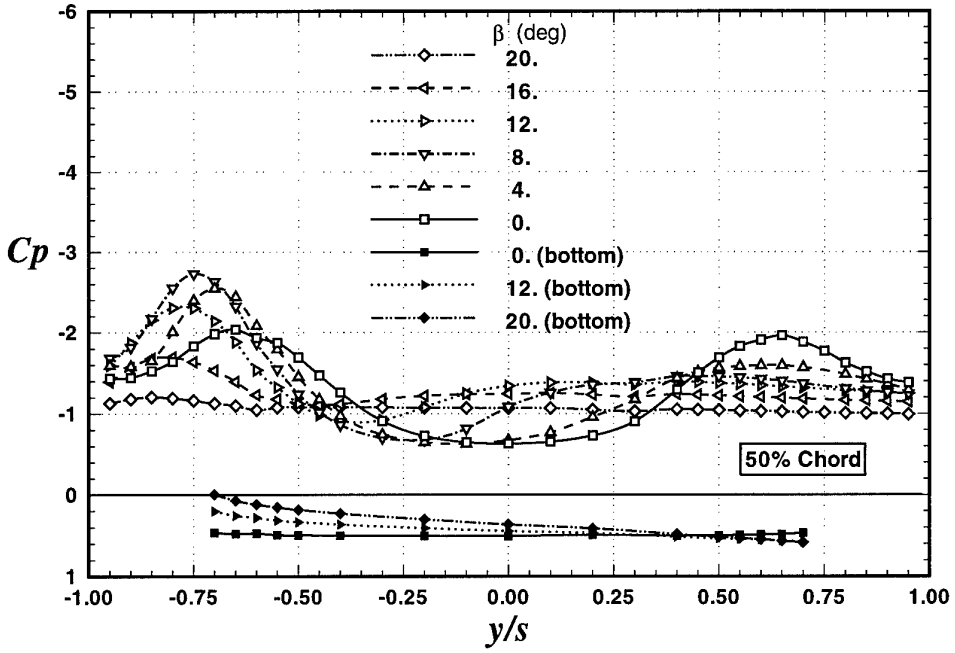

Figure 35: Effect of β on C_p-distribution at 30 and 50% chord

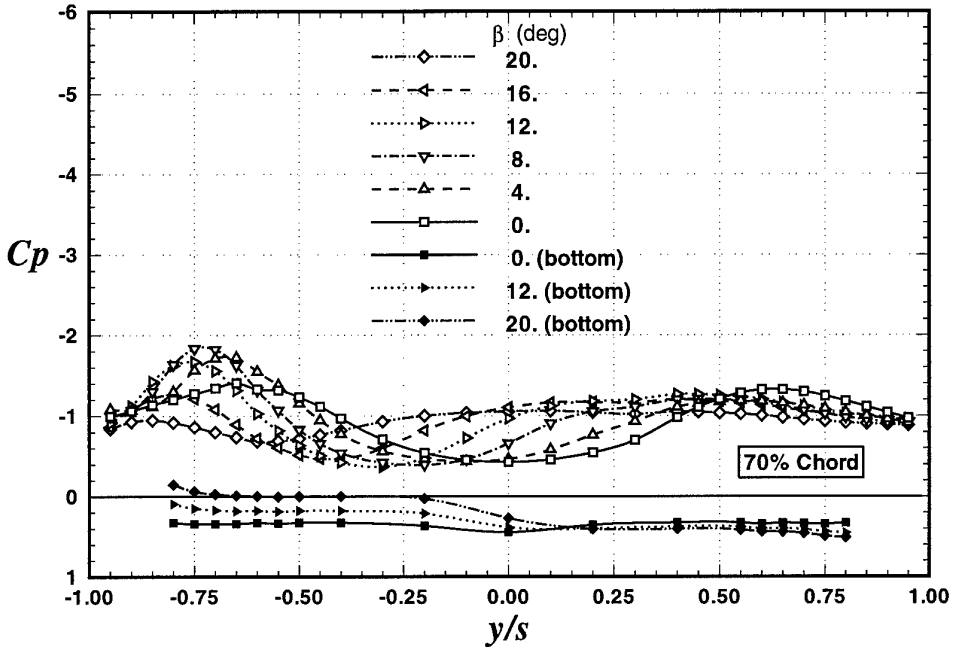

Figure 36: Effect of β on C_p-distribution at 70% chord

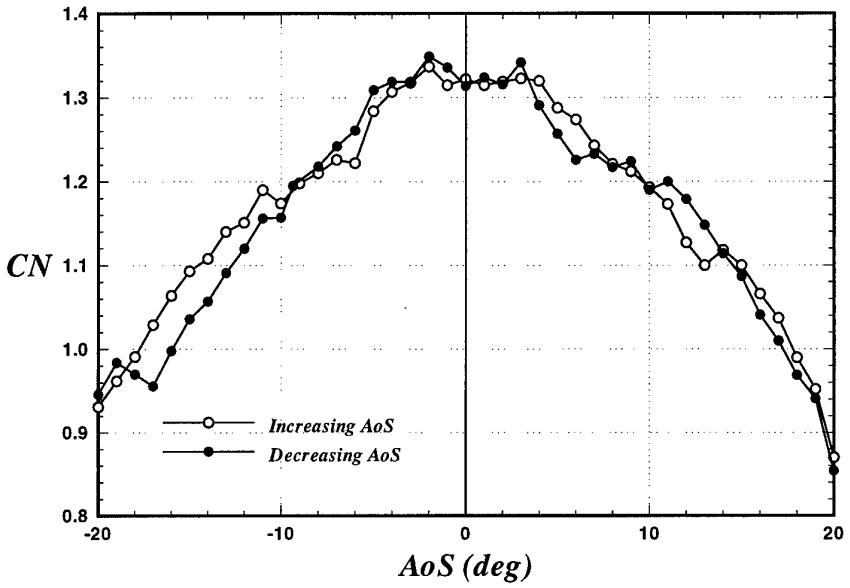

a. Effect of β on normal-force coefficient

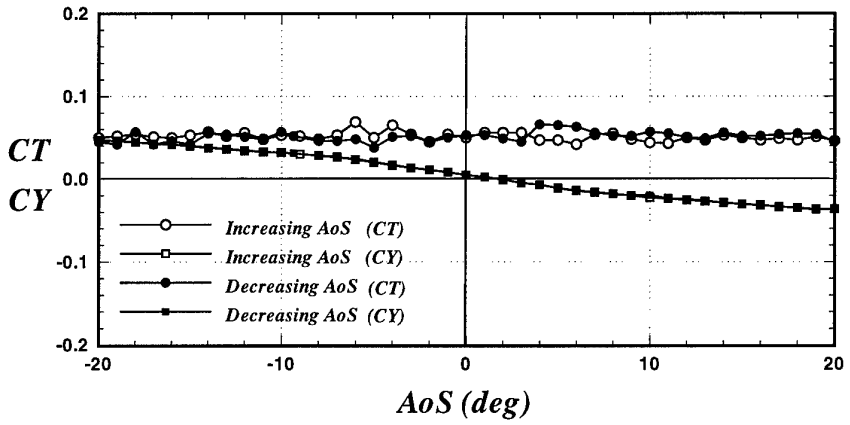

b. Effect of β on tangential and lateral-force coefficient

Figure 37: Effect of β on force coefficients (data set 1)

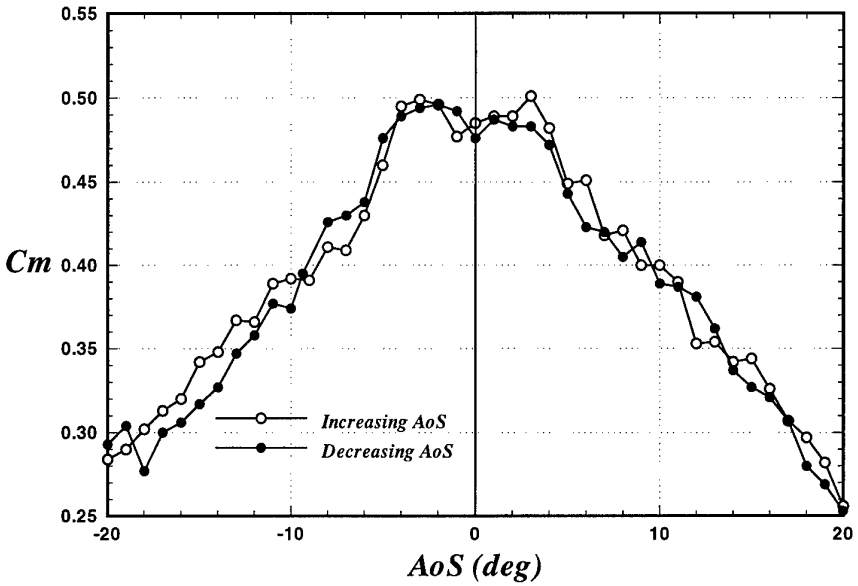

a. Effect of β on rolling-moment coefficient

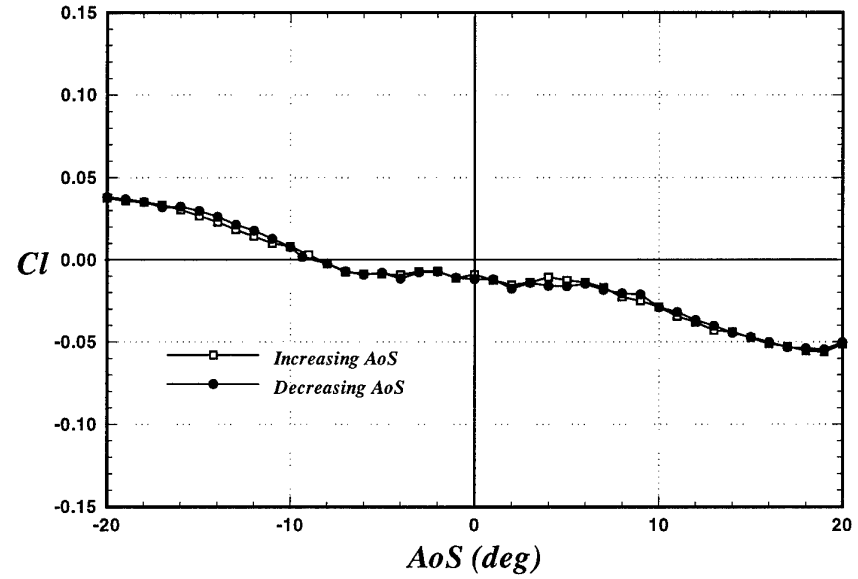

b. Effect of β on pitching-moment coefficient

Figure 38: Effect of β on moment coefficients (data set 1)

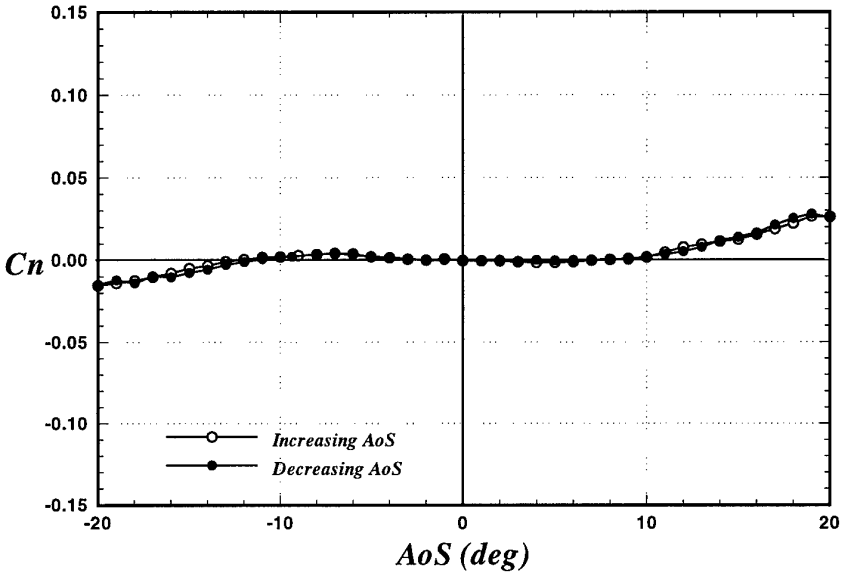

Figure 39: Effect of β on yawing-moment coefficient (data set 1)

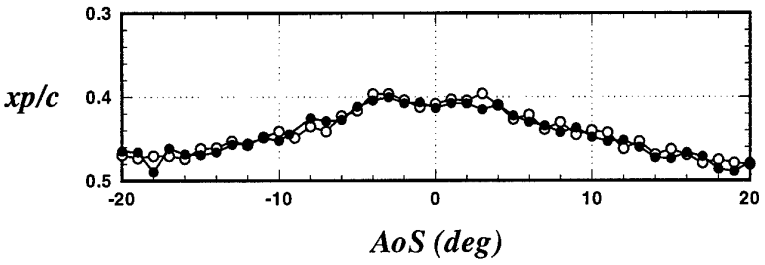

a. Effect of β on chordwise location of center of pressure

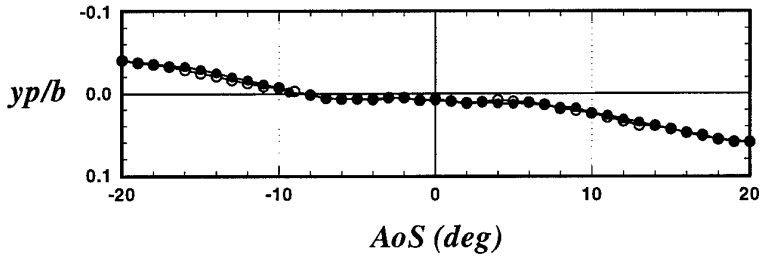

b. Effect of β on lateral position of center of pressure

Figure 40: Effect of β on center of pressure location (data set 1)

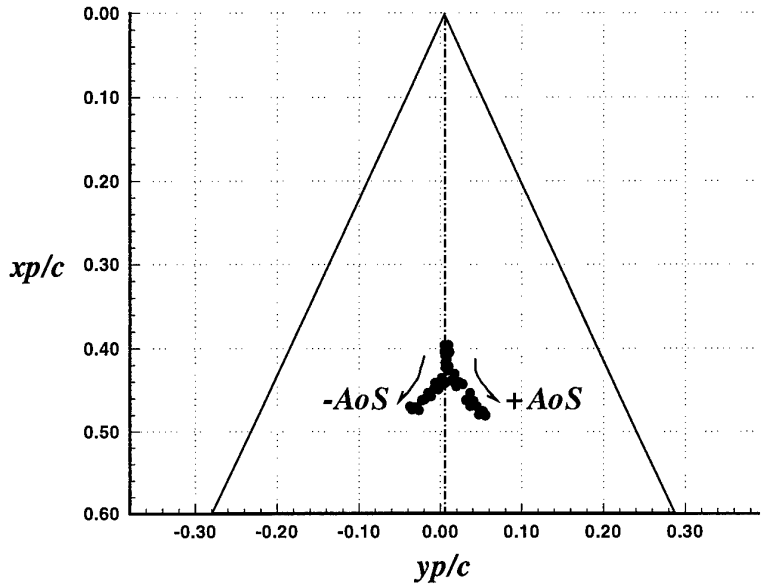

Figure 41: Effect of β on center of pressure location (Continued)

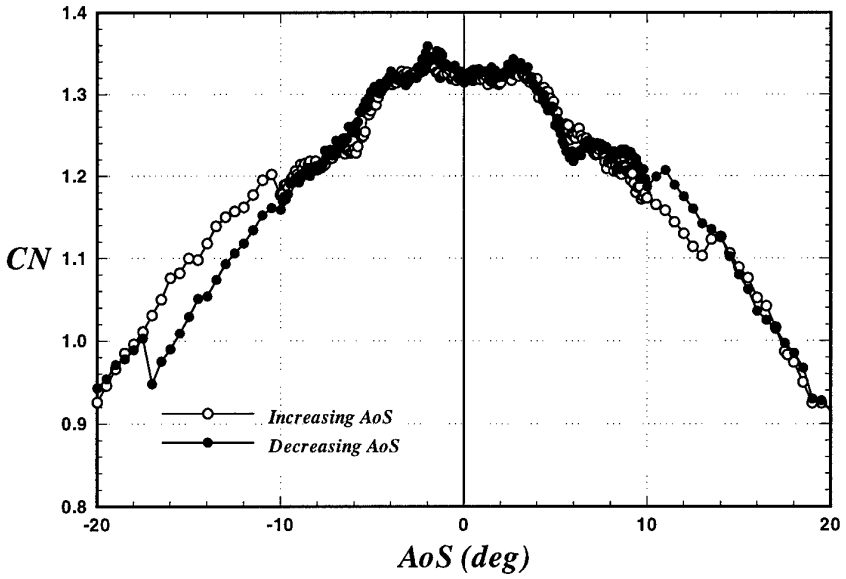

Figure 42: Effect of β on C_N (data set 2)

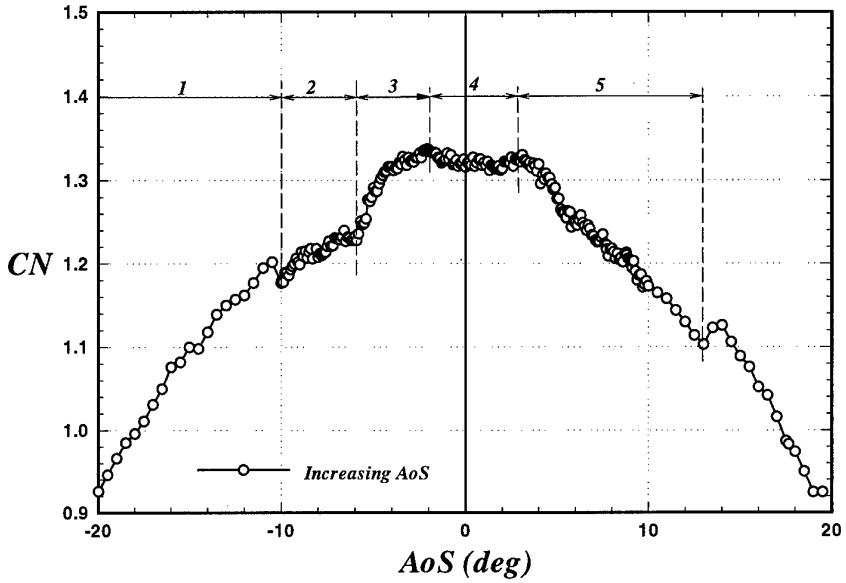

a. β increasing from -20 to +20 deg

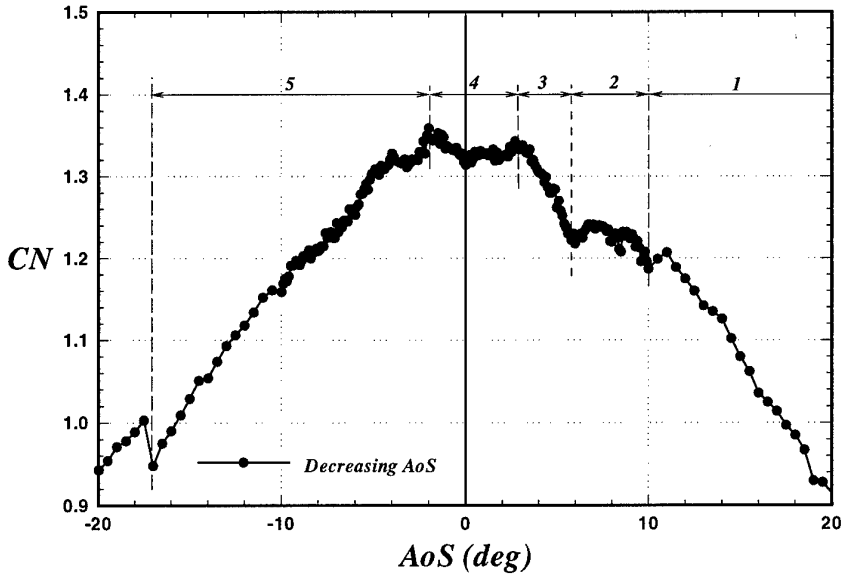

b. β decreasing from +20 to -20 deg

Figure 43: Distinct regions in C_N-curves (data set 2)

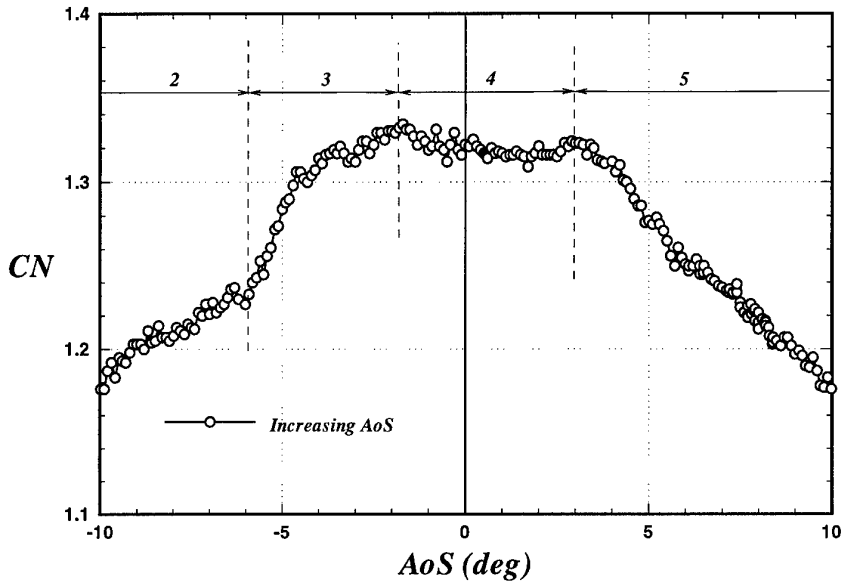

a. β increasing from -10 to +10 deg

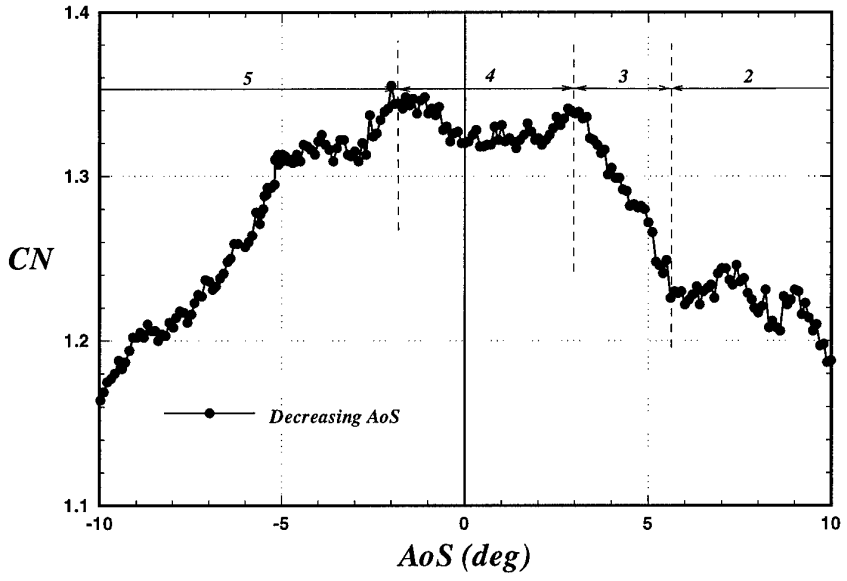

b. β decreasing from +10 to -10 deg

Figure 44: Distinct regions in C_N-curves (data set 3)

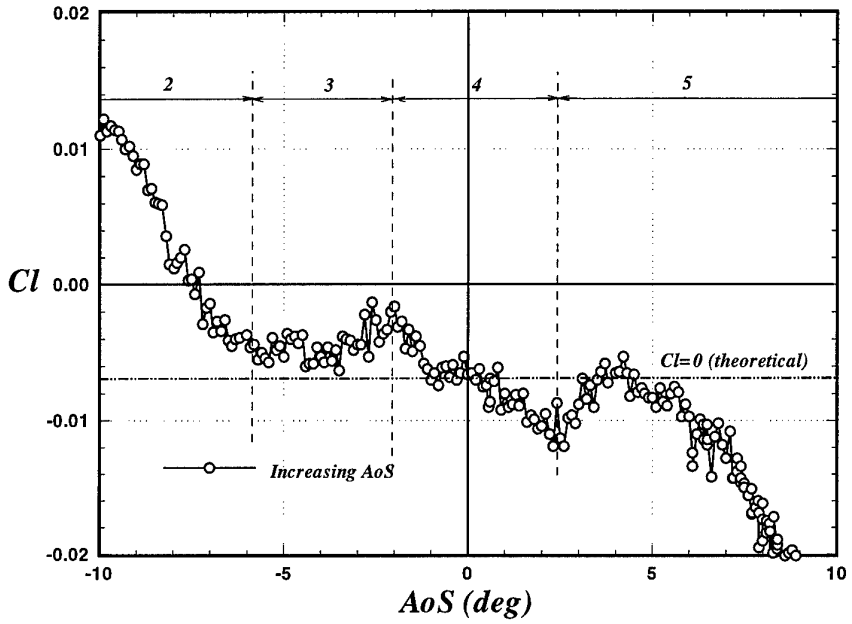

a. β increasing from -10 to +10 deg

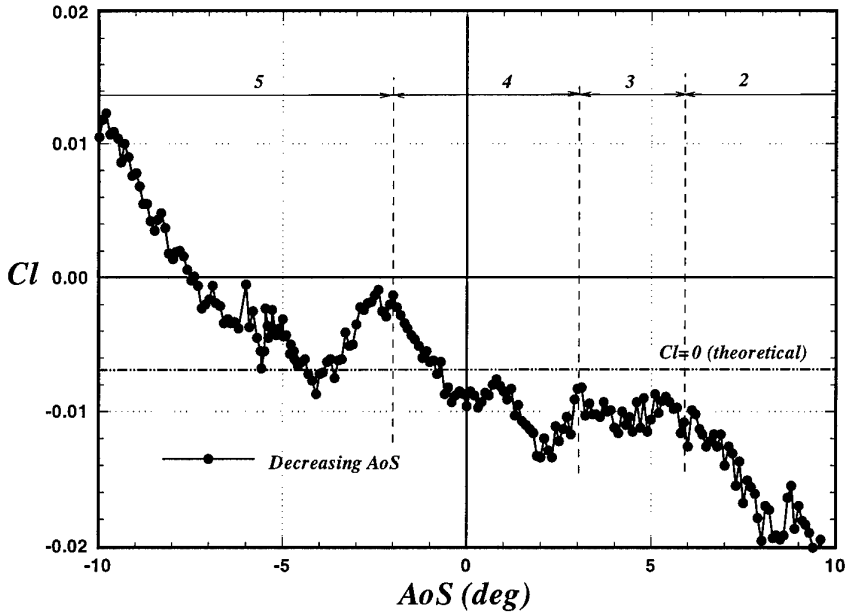

b. β decreasing from +10 to -10 deg

Figure 45: Distinct regions in C_l-curves (data set 3)